Dynamics of Telomeres and Promyelocytic Leukemia Nuclear Bodies in a Telomerase-negative Human Cell Line

Thibaud Jegou,*† Inn Chung,*† Gerrit Heuvelman,*† Malte Wachsmuth,‡ Sabine M. Görisch,§ Karin M. Greulich-Bode,∥ Petra Boukamp,∥ Peter Lichter,§ and Karsten Rippe*†

*Research Group Genome Organization and Function, §Division of Molecular Genetics, and ∥Division of Genetics of Skin Carcinogenesis, Deutsches Krebsforschungszentrum, 69120 Heidelberg, Germany; †BioQuant, 69120 Heidelberg, Germany; and ‡European Molecular Biology Laboratory, Cell Biology/Biophysics Unit, 69117 Heidelberg, Germany

Telomerase-negative tumor cells maintain their telomeres via an alternative lengthening of telomeres (ALT) mechanism. This process involves the association of telomeres with promyelocytic leukemia nuclear bodies (PML-NBs). Here, the mobility of both telomeres and PML-NBs as well as their interactions were studied in human U2OS osteosarcoma cells, in which the ALT pathway is active. A U2OS cell line was constructed that had *lac* operator repeats stably integrated adjacent to the telomeres of chromosomes 6q, 11p, and 12q. By fluorescence microscopy of autofluorescent LacI repressor bound to the *lac*O arrays the telomere mobility during interphase was traced and correlated with the telomere repeat length. A confined diffusion model was derived that describes telomere dynamics in the nucleus on the time scale from seconds to hours. Two telomere groups were identified that differed with respect to the nuclear space accessible to them. Furthermore, translocations of PML-NBs relative to telomeres and their complexes with telomeres were evaluated. Based on these studies, a model is proposed in which the shortening of telomeres results in an increased mobility that could facilitate the formation of complexes between telomeres and PML-NBs.

INTRODUCTION

Telomeres are specialized chromatin structures at the end of linear chromosomes, in which repetitive DNA sequences (5'-TTAGGG-3' in vertebrates) associate into a nucleoprotein complex (de Lange *et al.,* 2006). This complex—the "telosome"—protects the chromosome ends from degradation and genomic rearrangement and includes the "shelterin" proteins TRF1, TRF2, and POT1 that directly recognize the TTAGGG repeat sequence (de Lange, 2005; Bertuch and Lundblad, 2006; Croy and Wuttke, 2006; Blasco, 2007). Because of incomplete DNA synthesis at the chromosome ends, 50–200 base pairs of telomeric DNA are lost during each replication cycle (Harley *et al.,* 1990; Martens *et al.,* 2000). After ~60–80 cell divisions telomere repeats are shortened from a typical initial length of 10–15 kb in human cells to ~5 kb and below, which triggers cell senescence or apoptosis (Harley *et al.,* 1990; Martens *et al.,* 2000; Blasco, 2007). Accordingly, tumor cells need to compensate the loss of their telomere repeats in order to sustain an unlimited proliferative potential. In most cases this is accomplished by

reactivating telomerase, a reverse transcriptase that synthesizes telomeric repeats at the chromosome ends (Greider and Blackburn, 1985; Chan and Blackburn, 2004; Collado *et al.,* 2007; Johnson and Broccoli, 2007). However, a fraction of ~10–15% of tumors is able to maintain their telomeres in the absence of telomerase activity. This process has been designated as alternative lengthening of telomeres (ALT; Bryan *et al.,* 1995; Neumann and Reddel, 2006; Johnson and Broccoli, 2007). In yeast and mammals, it has been shown that the ALT mechanism involves homologous recombination events between telomere repeats (Dunham *et al.,* 2000; Kass-Eisler and Greider, 2000; Lundblad, 2002; Muntoni and Reddel, 2005). It is characterized by a number of features that include 1) a highly heterogeneous telomere length distribution ranging from <3 to >50 kb (Bryan *et al.,* 1995; Perrem *et al.,* 2001; Scheel *et al.,* 2001; Neumann and Reddel, 2006), 2) the presence of circular and linear extrachromosomal telomeric repeat DNA (ECTR-DNA) of up to ~60 kb in size (reviewed in Neumann and Reddel, 2006), and 3) a particular class of promyelocytic leukemia nuclear bodies (PML-NBs) that form specific complexes with telomeres termed ALT-associated PML bodies (APBs; Yeager *et al.,* 1999).

PML-NBs are mobile nuclear organelles that have been implicated in multiple biological functions including transcription, DNA replication and repair, apoptosis, cellular proliferation, senescence, and tumor suppression (Dellaire and Bazett-Jones, 2004; Takahashi *et al.,* 2004; Bernardi and Pandolfi, 2007). The DNA recombination and DNA repair–related activities localized in the PML body components of the APB complex are regarded as essential for telomere lengthening via the ALT mechanism (Yeager *et al.,* 1999;

Nabetani *et al.,* 2004; Neumann and Reddel, 2006). Several genes potentially involved in the ALT pathway were recently identified using an RNAi-based approach (Jiang *et al.,* 2007). These are related to PML body formation (PML) and DNA repair (MRE 11, Rad50) as well as telomere metabolism (TRF1 and TRF2). Furthermore, it has been demonstrated that the SMC5/6 (structural maintenance of chromosomes) complex is present in APBs and that the SUMO (small ubiquitin-like modifiers) ligase activity of the MMS21 component of SMC5/6 is required for APB formation (Potts and Yu, 2007).

Both telomeres and PML-NBs can translocate in the nucleus, and the findings mentioned above point to a crucial role of telomere–telomere and telomere–PML-NB interactions for the ALT mechanism. Thus, it is essential to determine the factors that govern their mobility in cell lines that maintain their telomeres via the ALT pathway. Previously, we have proposed that the dynamic chromatin organization of the interphase nucleus is responsible for the confined translocation of mobile nuclear subcompartments like PML bodies and their targeting to certain regions of the nucleus (Görisch *et al.,* 2004). The apparent mobility of nuclear particles and chromatin loci as described by their diffusion coefficient and accessible space is highly dependent on the observation period because of the multiscale organization of chromatin as discussed in detail elsewhere (Wachsmuth *et al.,* 2008). Accordingly, chromatin loci show multiscale movements as inferred from the analysis of different time regimes (Marshall *et al.,* 1997; Vazquez *et al.,* 2001; Chubb *et al.,* 2002; Levi *et al.,* 2005; Chuang and Belmont, 2007).

In general, it appears that both the translocations of chromosomal loci as well as those of nuclear bodies are confined to 200–300 nm, with apparent diffusion coefficients in the range of 10^{-4} to 10^{-5} μm^2 s^{-1} on the minute-to-hour time scale (Wachsmuth *et al.,* 2008). These relatively slow and confined diffusive movements would make interactions between telomeres and PML-NBs a relatively slow process. Accordingly, an increase of their ability to translocate in the nucleus could significantly promote interactions. Previously, a fluorescently tagged peptide nucleic acid (PNA) probe directed against telomere repeats was used to gain insight into the in vivo mobility of telomeres and their interaction with PML bodies in the osteosarcoma U2OS cell line that maintains telomeres via the ALT mechanisms (Molenaar *et al.,* 2003). The vast majority of the visible telomeres exhibited constrained movements within nuclear regions of ~0.5-μm radius, whereas a small fraction of telomeres exhibited an increased mobility. In addition, some telomeres displayed transient interactions indicative of the formation of dynamic telomere clustering that might be relevant for the recombination events associated with the ALT mechanism. Although the labeling of telomere repeats with a fluorescent PNA has the advantage of visualizing a large fraction of telomeres in the U2OS cell line, this approach also has some limitations. First, very short telomeres in ALT cells, which are particularly relevant for inducing cell senescence or apoptosis, can hardly be detected because the fluorescent signal is not sufficient for tracing them (Perrem *et al.,* 2001; Scheel *et al.,* 2001). Second, the fluorescent labels cannot be assigned to a specific chromosome because all repeats of sufficient length are visualized. Third, signals arising from telomeres cannot be distinguished from those that originate from hybridization of the probe to ECTR-DNA. The same restriction would apply to the in vivo labeling of telomere repeats via a bound autofluorescent construct of a shelterin protein such as TRF1 or TRF2 (de Lange, 2005). An alternative approach to tag chromosomal loci makes use of the high-affinity binding of bacterial LacI repressor protein fused with autofluorescent green fluorescent protein (GFP-LacI) to repeats of *lac* operator (*lac*O) sequences stably integrated into the genome (Robinett *et al.,* 1996; Straight *et al.,* 1996). This *lac*O/GFP-LacI tagging of genomic loci has been applied in a number of studies of chromatin structure and dynamics in living cells as reviewed recently (Chuang and Belmont, 2007). Here, the mobility of telomeres and their interaction with PML-NBs in U2OS cells was monitored by fluorescence microscopy after labeling of integrated *lac*O repeats with GFP-LacI/mRFP1-LacI. The experiments yielded a comprehensive description of telomere mobility on different time scales and identified differences in the accessible nuclear space. In conjunction with studies of PML-NBs a model is proposed in which the shortening of telomeres results in an increased mobility that could facilitate the formation of APBs.

MATERIALS AND METHODS

### Cell Culture and Generation of Clones with Stable lacO Array Integrations

Cells of the human U2OS osteosarcoma cell line (HTB-96) were grown in DMEM (Invitrogen, Carlsbad, CA) containing 10% FCS (PAA Laboratories, Linz, Austria). Cell lines with stably integrated *lac*O arrays were constructed by cotransfection of the pLAU 43 vector containing ~240 *lac*O repeats, provided by David Sherratt (University of Oxford, Oxford, United Kingdom) (Lau *et al.,* 2003), together with the neomycin resistance-coding vector pcDNA3.1 (Invitrogen). Selection was conducted with 750 μg/ml G418, and stable cell clones were picked and cultured for 1 wk in 96-well plates. The surviving cell clones were then screened for *lac*O integrations by transfection with GFP-LacI, which was generated from an mRFP1-LacI construct provided by Cristina Cardoso (University of Darmstadt, Darmstadt, Germany). For in vivo imaging of U2OS clones that had *lac*O arrays stably integrated into the genome, cells were seeded on coverslips or in Lab-Tek chambers (Nunc, Roskilde, Denmark) that were covered with Matrigel (BD Biosciences, San Jose, CA) and cultured for 2 d to achieve a stable attachment to the surface. The cells were transiently transfected ~17 h before the experiment with Fugene 6 (Roche Diagnostics, Mannheim, Germany) or Effectene (Qiagen, Hilden, Germany), and various plasmid vectors. These included N-terminally tagged GFP/mRFP1-LacI and GFP/mRFP1-PML III as used previously (Görisch *et al.,* 2004) or provided by Peter Hemmerich (Leibniz Institute for Age Research, Jena, Germany) (Weidtkamp-Peters *et al.,* 2008), proliferating cell nuclear antigen (PCNA)-GFP/cyan fluorescent protein (CFP) from Cristina Cardoso (Leonhardt *et al.,* 2000), H2A-mRFP1 derived from H2A-YFP (yellow fluorescent protein; Fejes Tóth *et al.,* 2004), and a GFP-TRF2 construct. The latter was obtained by amplifying the human TRF2 cDNA sequence by PCR with an upstream forward primer containing an HindIII restriction site and a downstream reverse primer containing a BamHI restriction site. The PCR product was then cloned in the pEGFP-C1 vector (Clontech, Palo Alto, CA). Fixation of cells was conducted with 4% paraformaldehyde (PFA) in PBS buffer and incubation for 12 min at room temperature. Chromatin was stained either by mounting cover slips in Vectashield containing DAPI (Vector Laboratories, Peterborough, United Kingdom) or by staining with solution of 1 μM TO-PRO 3 (Invitrogen).

Fluorescence Microscopy

Long-term observations were conducted with a Leica TCS SP2 confocal laser scanning microscope (CLSM; Deerfield, IL). Z-stacks of 12–20 frames with 0.3-μm spacing were collected every 5 min for 3–5 h. The Leica CLSM was used with an objective heater and an environment chamber for maintaining the temperature at 37°C and the CO_2 concentration at 5%. For high-speed imaging a Perkin Elmer-Cetus Ultra-View or a Perkin Elmer-Cetus ERS-FRET spinning disk system (Norwalk, CT) with a Tokai Hit chamber (Fujinomiya, Japan) at 37°C temperature were used. These experiments were conducted either with medium containing 10 mM HEPES at pH 7.4 in the absence of CO_2 or with L-15 (Leibovitz) medium (PAA). For minute time-scale experiments Z-stacks were collected every 10 s for 15 min. For experiments with millisecond time resolution, cells were selected that had the three *lac*O loci in the same focal plane, and images were acquired for 5 min with a time resolution between 50 and 100 ms.

Metaphase Spreads

Cells were incubated with 0.5 μg ml^{-1} colcemid (CaryoMax, Invitrogen) for 90 min at 37°C, detached with trypsin, pelleted by centrifugation, and resuspended in 500 μl fresh medium. Then 10 ml of a prewarmed 75 mM KCl solution was added, and the cells were incubated for 30 min at 37°C, pelleted, and resuspended in 500 μl KCl solution. Fixation was conduced by addition
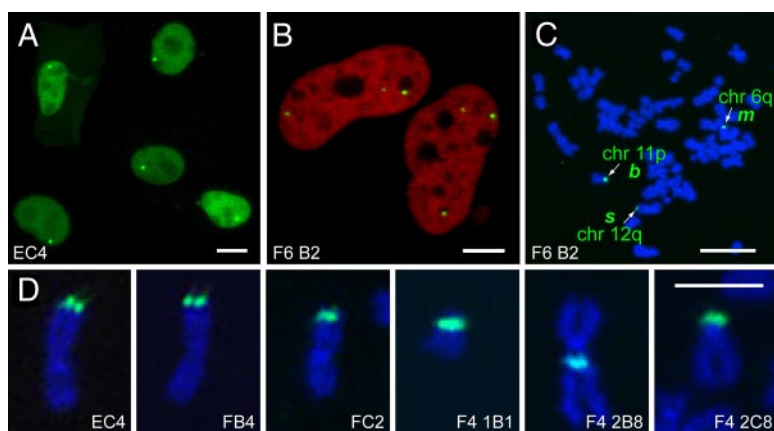
Figure 1. U2OS cell clones with a stably integrated *lac*O array. Scale bar, (A) 10 μm; (B–D) 5 μm. (A) Cell clone EC4 with a single *lac*O integration observed in vivo after transient transfection with GFP-LacI. (B) The clone F6B2 showed three distinct integration sites that could be identified due to their differences in size. Cells were transiently transfected with GFP-LacI and fixed and DNA-staining was with TO-PRO 3. (C) The chromosomal integration site of *lac*O arrays was determined by metaphase FISH using a 6-FAM fluorescently labeled oligonucleotide probe coding for the *lac*O sequence and DNA counter-staining with DAPI. The *lac*O arrays were found to integrate at the telomeric regions of chromosomes 11p, 6q, and 12q. See also Supplemental Figure S1 for mFISH analysis. (D) Metaphase chromosomes from different cell clones with a stably integrated *lac*O array showed a highly preferred integration at the telomeres (29/30 clones).

of 10 ml ice cold solution of methanol and glacial acetic acid at a 3:1 vol/vol ratio, and cells were incubated 30 min at −20°C, pelleted, washed five times, resuspended in 500 μl fixation solution, and deposited onto the slides.

Fluorescence In Situ Hybridization, Multicolor FISH, and PNA FISH

Chromosome spreads were treated with a solution containing 250 μg ml^{-1} pepsin and 10 mM HCl for 2–3 min, washed with PBS buffer, and refixed with PFA. After an additional wash with PBS buffer, slides were dehydrated by series of ethanol washes (70, 90, and 100% ethanol) each with 5-min incubation time. DNA was denatured by incubating the slides for 5 min at 72°C in a solution containing 70% deionized formamide and 2× SSC buffer at pH 7. Cells were immediately dehydrated by another series of ethanol washes as described above. After drying of the slide, 200 ng of a fluorescein-labeled oligonucleotide probe coding for the *lac*O sequence was added onto the sample in a 30 μl solution containing 1.5 M NaCl and 0.25 M Na-acetate at pH 7. A coverslip was added and sealed with fixogum, and slides were incubated overnight at 37°C in a wet chamber, washed in 4× SSC, 0.2% Tween 20 for 5 min, and mounted in Vectashield. For simultaneous staining of *lac*O arrays and telomere repeats a FISH (fluorescence in situ hybridization) label of the *lac*O sequence was first conducted as described above. Then a telomere PNA FISH was conducted with a Cy3-labeled (CCCTAA)$_3$ PNA probe according to the protocol of the manufacturer (Dako, Glostrup, Denmark). Chromosomes spreads from the preceding *lac*O FISH experiment were relocated and imaged. The multicolor FISH (mFISH) analysis was performed using the SpectarVysion 24 color chromosome paint assay and Quips Spectra Vysion software (Vysis, Downers Grove, IL). Images were acquired using an Axioplan 2 microscope (Zeiss, Jena, Germany) together with a Sensys CCD camera (Photometrix, Tucson, AZ). After the mFISH analysis, slides were incubated two times for 10 min in a 4× SSC solution containing 0.1% Tween 20, washed two times with 2× SSC buffer, and dehydrated by a series of ethanol washes. Then labeling of the *lac*O arrays by FISH was conducted as described above, and chromosome spreads were relocated and imaged.

Mobility Measurements

For single-particle tracking maximum intensity projections of three-dimensional (3D) stacks along the Z-axis were used. It is noted that for an isotropic movement of the particle in 3D the value determined for the diffusion coefficient D from projections to 2D will be the same as that obtained from the analysis of 3D data sets as described previously (Görisch *et al.,* 2004). The coordinates for the movements of the GFP-LacI–labeled *lac*O arrays were determined with ImageJ 1.36 (NIH, http://rsb.info.nih.gov/ij/) using the SpotTracker software for tracking particle translocations with subpixel resolution (Sage *et al.,* 2005). Alignment of the cell nucleus was made with the StackReg plug-in (Thévenaz *et al.,* 1998) or with a self-written MatLab (Math-Works, Natick, MA) program that uses an image correlation algorithm to maximize the image overlap between successive images. From the x-y coordinates of the tracked spots either the mean squared displacement (MSD) or the mean squared distance change (MSΔD or $<\Delta$d2$>$) between two labeled telomeres was determined. The latter approach was developed here to improve the accuracy and is described in detail in Supplemental Materials. For the mobility analysis the three telomeres in clone F6B2 were tracked on different time scales in 22 cells (second time scale, Δt = 50–100 ms), 18 cells (minute time scale, Δt = 8–15 s), and 44 cells (hour time scale, Δt = 5 min). For the mobility analysis only cells were evaluated that were stably attached to the surface and showed little deformation of their shape.

RESULTS

Characterization of U2OS Cell Lines with Integrated lacO Arrays

A series of 30 cell clones was generated that had *lac*O repeats stably integrated into the genome. The cell clones were distinct with respect to the chromosomal integration loci and the number of operator integrations. The *lac*O arrays were visualized in vivo by transient transfection with GFP-LacI or mRFP1-LacI constructs. Examples are shown in Figure 1. Because also the unbound GFP-LacI/mRFP1-LacI repressor remained in the nucleus, it provided a nuclear counterstaining during the in vivo observations (Figure 1A), whereas for fixed cells a DNA staining with DAPI or TO-PRO 3 was conducted (Figure 1B). The sites of the *lac*O integrations were determined by FISH (Figure 1C). Remarkably, all except one of the clones had an integration at the telomeres (Figure 1D). This observation indicates a high DNA recombination activity at the telomeres in U2OS cells that use the ALT mechanism for maintaining their chromosomal ends. The experiments reported in the following used clone F6B2 with *lac*O integrations sites at three different telomeres (Figure 1B). Because the U2OS cell line displayed a complex karyotype, the genomic integration sites were identified from metaphase FISH (Figure 1C) and mFISH experiments (Supplemental Figure S1) followed by a rehybridization with the fluorescently labeled *lac*O probe. The integration sites were found to be at the telomere regions of chromosomes 6q, 11p, and 12q. Because of the different repeat numbers of the *lac*O integrations, the three chromosomes could be distinguished in vivo. The biggest spot *b* is on chromosome 11p, the medium sized spot *m* is on chromosome 6q, and the smallest spot *s* is on chromosome 12q. The three loci had apparent diameters of 0.74 ± 0.09 (*b*), 0.54 ± 0.05 (*m*), and 0.42 ± 0.05 μm (*s*), respectively. Assuming an average nucleosome concentration of 0.14 mM and a 200-base pair nucleosome repeat length (Weidemann *et al.,* 2003), this would correspond estimates of 3.6, 1.4, and 0.7 Mb of DNA. Because of the diffraction-limited resolution of the optical system used here, the true dimensions of the array are smaller. This is inferred from comparitive measurements of array sizes by spatially modulated illumination microscopy (Reymann *et al.,* 2008). On the other hand the chromatin density of the *lac*O arrays appears to be above average.

Because the metaphase chromosomes are in a highly condensed chromatin state, the spatial overlap of the *lac*O integration site with the telomere repeat does not exclude the presence of a significant amount of DNA between the two
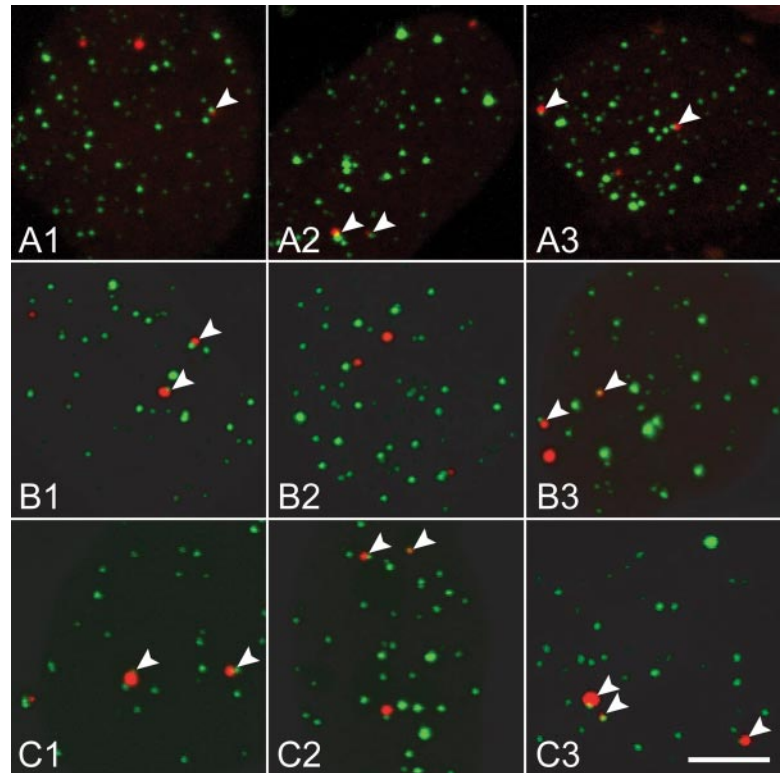
Figure 2. Integrated *lac*O arrays colocalize with telomeres during interphase. Maximum intensity projections of confocal picture stacks of the F6B2 clone are shown. The white arrows indicate *lac*O arrays that colocalize with the telomere signal in a single focal plane. The analysis was conducted with three different labeling methods. In all three methods, a fraction of the *lacO* arrays were without a detectable telomere signal indicative of very short telomere repeats. Scale bar, 5 μm. (A) The *lac*O repeats were detected by transfecting the cells with GFP-LacI, and telomeres were stained by FISH with a Cy3-labeled (CCCTAA)₃ PNA probe. (B) Cells were transfected with mRFP1-LacI and endogenous TRF2 was detected by immunostaining with an Alexa-488−coupled secondary antibody. (C) Cells were cotransfected with mRFP1-LacI together with GFP-TRF2 for labeling of living cells.

loci. We therefore investigated the localization of *lac*O arrays with respect to the telomeres in decondensed chromosomes during interphase. The *lac*O arrays were labeled with GFP-LacI or mRFP1-LacI, whereas the telomeres were visualized by three different approaches: 1) FISH using a Cy3-labeled PNA probe directed against the telomere repeats (Figure 2A). 2) Immunostaining of endogenous TRF2 protein that binds with high specificity to the (TTAGGG)ₙ sequence (de Lange, 2005; Figure 2B). 3) In vivo labeling with GFP-TRF2, which was introduced by cotransfection with an mRFP1-LacI vector (Figure 2C). All three methods showed essentially the same results. The three *lac*O array integrations were located directly adjacent to the telomere repeat sequence and no differences between arrays *b*, *m,* and *s* were apparent. Live imaging with cells cotransfected with mRFP1-LacI together with GFP-TRF2 demonstrated that the colocalization was stable through a period of several hours and that the *lac*O arrays showed a highly correlated movement with the GFP-TRF2 label (Supplemental Movie 1). Thus, tracing the *lac*O array in vivo is an appropriate representation of the mobility of the adjacent telomere. It is also noted that the intensity of both the PNA and the GFP-TRF2 fluorescence signal correlates with the telomere repeat length (Lansdorp *et al.,* 1996). Thus, the absence of a PNA/GFP-TRF2 signal close to a given *lac*O label is indicative of a very short telomere repeat at this chromosome (Perrem *et al.,* 2001; Scheel *et al.,* 2001).

The mobility analysis presented here was conducted with cells in the middle of G1 to early S phase. From experiments with an H2A-YFP label it was apparent that shortly after cell division in early G1 phase the cells were more rounded and showed relatively large translocations on the surface. These cells in early G1 phase were excluded because we selected only flat cells with fully decondensed chromosomes that were stably attached to the surface. Using the replication associated protein PCNA as a cell cycle marker, we identified

an arrest in early S phase before replication of the *lac*O arrays in cotransfection experiments with mRFP1-LacI and PCNA-CFP (Supplemental Movie 2). In the absence of LacI repressor no effect on cell cycle progression was observed with respect to the parental U2OS cell line without the *lac*O integrations (data not shown). Thus, we concluded that LacI bound to the *lac*O repeats blocked DNA polymerase at the late replicating telomeric regions (Gilson and Geli, 2007). This is consistent with the finding that LacI or TetR repressors tightly bound to arrays of their operator sites efficiently stall the replication fork in *Escherichia coli* (Possoz *et al.,* 2006). As determined from the characteristic PCNA distribution pattern, 62 ± 5% of the cells with three *lac*O array labels were in G1 phase, whereas the remaining 38 ± 4% displayed PCNA in replication foci. When evaluating the *lac*O mobility in G1 cells with those in early S phase (either in separate cells or in cells that progressed from G1 to S phase, Supplemental Movie 2), no correlation of mobility and cell cycle state was observed.

Theoretical Framework for Evaluating the Telomere Mobility

The accurate measurement of the MSD in the nucleus is difficult because the cell itself can move during the measurement and the alignment to correct for this is fraught with difficulties. Accordingly, an alternative method was developed here that evaluated changes in the distance between two loci (Figure 3A). This approach was applied previously to analyze the mobility of *lac*O-tagged genomic loci but not in the context of a quantitative confined diffusion model (Marshall *et al.,* 1997; Vazquez *et al.,* 2001; Chubb *et al.,* 2002). A detailed derivation of the formalism used here is given in Supplemental Materials. If multiple particles/loci are present, the change in distance $\vec{d}(t) = \vec{p}_1(t) - \vec{p}_2(t)$ between the position $\vec{p}$ of two particles with indices 1 and 2 is given by Equation 1. In this regard, the mean squared difference in distance, MSΔD, referred to here also as [Δd²], is the sum of the mean squared
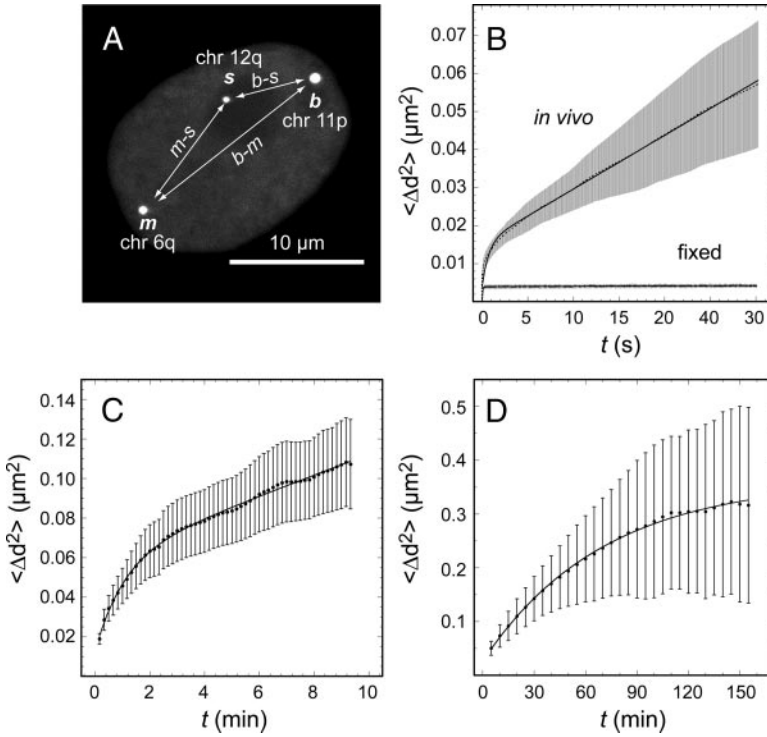
Figure 3. Average mobility of telomeres on the second, minute, and hour time scale. Images were recorded with a spinning disk or a point scanning CLSM. The fluorescent spots were tracked and the mean squared changes $\langle \Delta d^2 \rangle$ in the distance between two telomeres were plotted against time. Averages of 20–40 trajectories are shown in each panel. (A) The mobility analysis of clone F6B2 was conducted in vivo by measuring changes in the distances between the three loci. In this clone the three loci were distinct with respect to the number of integrated *lacO* repeats and are referred to as *b* (for big), *m* (for medium), and *s* (for small). The distances *b-m*, *b-s*, and *m-s* are indicated. Scale bar, 10 μm. (B) Images were taken with a time resolution between 50 and 100 ms for a total of 5 min (see Supplemental Movie 3). The corresponding tracing of fixed cells is also plotted. The curve is a fit of the data to the MC model (Equation 3). (C) Image stacks were taken every 8–15 s for 20 min (see Supplemental Movie 4). The curve is a fit of the data to the MC model (Equation 3). (D) Image stacks were acquired in 5-min time intervals for a total of 3–5 h min (see Supplemental Movies 5 and 6). The solid line is a fit of the data to a confined diffusion model (Equation 2).

displacement by diffusion, and MSD_{diff}, of the two particles under the condition that rotation of the cell can be neglected:

$$MS\Delta D(\Delta t) = \langle [\vec{d}(t + \Delta t) - \vec{d}(t)]^2 \rangle$$

$$= MSD_{1,diff}(\Delta t)\, MSD_{2,diff}(\Delta t) \quad (1)$$

This was found to be a valid assumption under the experimental conditions used here as inferred from the mean linear displacement of the difference of two spots (Supplemental Materials Equation S8). To describe the restricted mobility of particles in the nucleus we have previously introduced a so-called "moving corral" (MC) model (Görisch *et al.,* 2004). An analysis of the data on the mobility of *lacO* loci indicated that a similar approach was also appropriate to represent the mobility of telomeres on different length and time scales. In the MC model the overall mobility in *n* dimensions is determined by three parameters: The particle experiences fast but confined diffusion with a coefficient D_{fast} in a corral with radius r_c, and the corral can also translocate by free diffusion with a coefficient D_{slow}. This model was extended to derive the above parameters from the change in the distance between two particles that experience corralled diffusion. It was found that telomere mobility on the hour time scale could be described by a simplified model according to Equation 2 that contained only the diffusion term within the corral (corresponding to $D_{slow} = 0$ in Equation 3):

$$MS\Delta D_{cor} \approx \langle r_{c,1}^2 \rangle \cdot \left[1 - \exp\left(-\frac{2nD_{fast,1}\Delta t}{\langle r_{c,1}^2 \rangle}\right)\right] + \langle r_{c,2}^2 \rangle$$

$$\cdot \left[1 - \exp\left(\frac{2nD_{fast,2}\Delta t}{\langle r_{c,2}^2 \rangle}\right)\right] + c \quad (2)$$

The additional offset c represents the faster mobility contributions detected in the analysis of telomere mobility on the

second and minute time scale. The data obtained from measurements obtained with these shorter observation times were described by Equation 3. Here the translocation of the corrals by free diffusion with coefficient D_{slow} was included:

$$MS\Delta D_{MC} \approx (\langle r_{c,1}^2 \rangle + \langle r_{c,2}^2 \rangle)\left(1 + \frac{2n(D_{slow,1} + D_{slow,2})\Delta t}{(\langle r_{c,1}^2 \rangle + \langle r_{c,2}^2 \rangle)}\right)$$

$$\cdot \left[1 - \exp\left(\frac{2n(D_{fast,1} + D_{fast,2})\Delta t}{(\langle r_{c,1}^2 \rangle + \langle r_{c,2}^2 \rangle)}\right)\right] \quad (3)$$

The analysis based on Equations 2 and 3 was found to give more accurate and robust values for the mobility of the telomeres than those obtained from the analysis of a single telomere after correction for cell movements. Furthermore, a direct and faithful comparison of the telomere mobilities within the same cells could be made.

Telomere Mobility on Different Time Scales

The mobility of the three telomeres in clone F6B2 on the second, minute, and hour time scale was recorded with corresponding time resolutions of milliseconds, seconds, and minutes. The quantitative analysis of telomere mobility ($MS\Delta D$ vs. time) was conducted as described in the preceding paragraph from measurements of the distance changes between the three labeled loci in the F6B2 clone (Figure 3A). Experiments with fixed cells showed that the position determination with subpixel resolution had an accuracy of ~60 nm.

All telomeres displayed a fast movement in a region of ~80-nm radius (after subtraction of 60 nm) with $D_{sec} = 2 \cdot 10^{-3}\ \mu m^2\ s^{-1}$ (Figure 3B, Supplemental Movie 3), and further slower translocations in a radius of 150 nm with $D_{min} = 4 \cdot 10^{-4}\ \mu m^2\ s^{-1}$ (Figure 3C, Supplemental Movie 4). For the analysis of movements on the hour time scale telomeres were traced via the *lacO* label for 3–5 h. From these
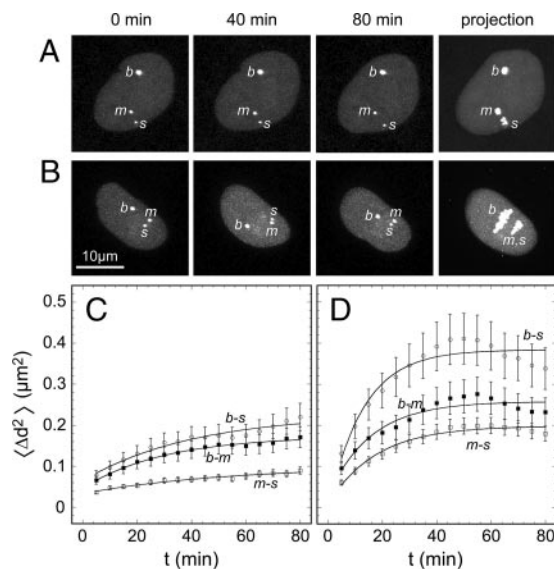
Figure 4. Differences in the mobility of telomeres on the hour time scale. (A) Cell with relatively slow-moving telomeres, which represents the majority of the observations (Supplemental Movie 5). (B) Cell showing two telomeres, *b* and *s*, that display extended translocations, whereas telomere *m* is only moderately mobile (Supplemental Movie 6). The quantitative analysis of distance variations between the three spots is shown in C for the cell in A and in D for the cell in B. The individual telomere mobility was calculated as described in the text from the distance changes between *b-s*, *b-m*, and *m-s*. The solid lines represent a fit to Equation 2, in which the translocations on the second and minute time scale are included as an offset.
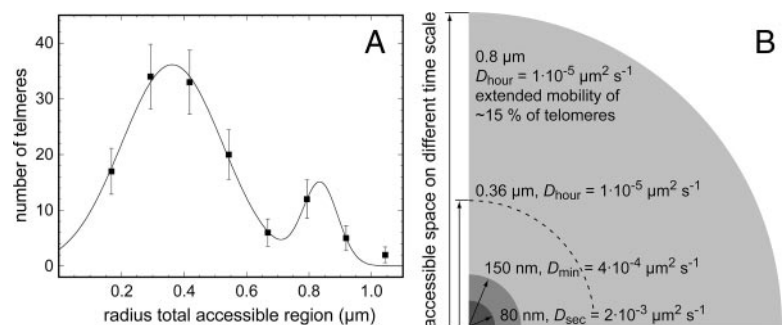
trajectories the MSΔD versus time of the big, medium, and small *lac*O arrays was determined. The confinement radii r_c, diffusion coefficients, and baseline offset for the three individual telomeres in each cell were determined from a global fit to Equation 2 (Figures 3D and 4, C and D) with a typical time-lapse series shown in Figure 4A. Some telomeres displayed an extended mobility with one particularly striking example shown in Figure 4B (see also Supplemental Movies 5 and 6). The existence of a bimodal mobility distribution for telomere translocations measured on the hour time scale was clearly apparent in the distribution of the radius of the accessible region (Figure 5A, n = 132). A lower mobility fraction of ~85% of the telomeres moved within a radius of 0.36 ± 0.16 μm average, whereas the mobility of the remaining ~15% was extended to a region with an average radius of 0.8 ± 0.1 μm. These values include the contributions of

the faster movements on the second and minute time scale that are represented by a baseline offset in Equation 2 that is added to the value of the parameter r_c to describe the extend of the total accessible region. For both populations the same average diffusion coefficient of $D_{hour} = 1 \cdot 10^{-5}$ μm² s⁻¹ was retrieved from the fit to Equation 2. No statistically significant differences between the telomere labels at 6q, 11p, and 12q were observed, indicating that the number of the *lac*O repeats integrated did not affect the mobility. Furthermore, the increased mobility on the hour time scale was not restricted to a certain telomere but was observed with a fraction of all three labeled telomeres (*b, m, s*) of clone F6B2. The results of the analysis of telomere translocations on different time scales are summarized in Figure 5B.
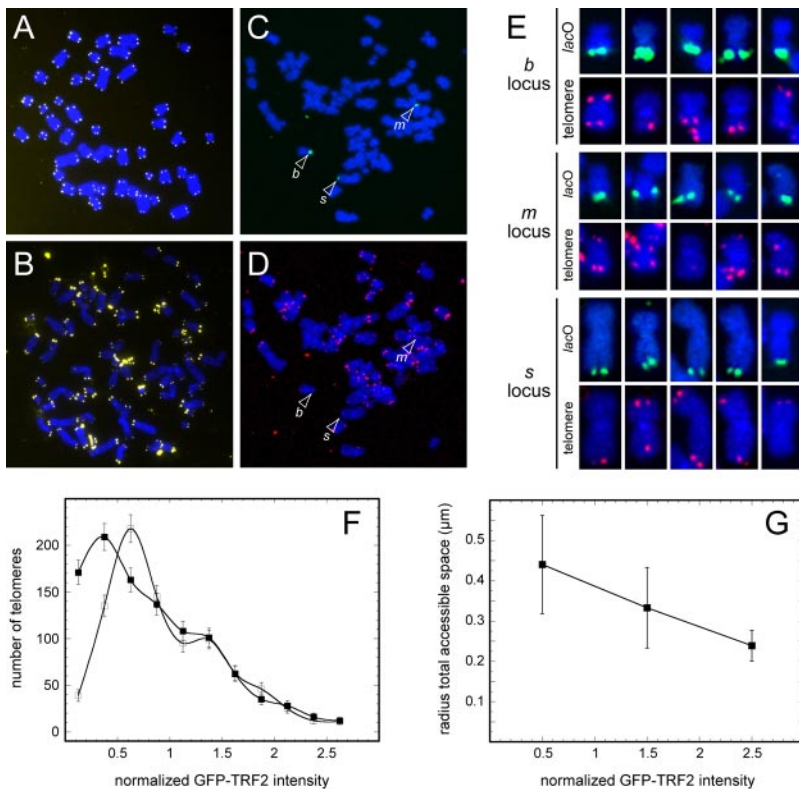
Analysis of Telomere Repeat Lengths
The telomere repeats were stained by FISH with a Cy3-labeled PNA probe specific for the (TTAGGG)$_n$ sequence (Figure 6). In a comparison of human lymphocytes (Figure 6A) with U2OS cells (Figure 6B) it is evident that the telomeres in the U2OS cells showed large variations in their repeat lengths as reflected by the intensity differences of the fluorescent label (see also Figure 2). In addition, the overall signal of the U2OS label was significantly higher than that of the lymphocytes, consistent with the increased average telomere length reported for this cell line (Scheel *et al.*, 2001). By conducting FISH experiments with a *lac*O probe (Figure 6C) followed by a rehybridization with the PNA probe against the telomeric repeats (Figure 6D), the telomere signal intensity was measured for the three *lac*O-labeled telomeres in the F6B2 clone. In Figure 6E examples for this type of analysis are presented. The *s, m,* or *b lac*O inserts displayed similar distributions of fluorescence intensities, indicating that the populations were not distinct with respect to the telomere repeat length. A large variability of signal intensity was observed at each of the three loci. For 20–30% of the *lac*O-labeled sites, the telomeres were undetectable by the PNA probe hybridization with a signal intensity less than twofold above the background value. A comparison of U2OS cells and the non-ALT HeLa cell line suggested that the presence of very short telomeres is pronounced in U2OS cells (Figure 6F). The distribution of telomere lengths in U2OS and HeLa cells was derived from the intensity of the GFP-TRF2 fluorescence signal (Figure 2C). For each GFP-TRF2 spot the ratio of its integrated intensity to the average value of all GFP-TRF2 telomere signals in a given cell was computed to normalize for differences between experiments. The distributions plotted in Figure 6F showed a much higher fraction of very short telomeres (GFP-TRF2 signal ≤0.5) in U2OS cells. It was then examined whether the telomere length

Figure 5. Mobility of telomeres in U2OS cells on different time scales. (A) Distribution of telomere translocations on the hour time scale as given by the radius of the total accessible region. The solid line represents a fit to a sum of two Gaussian functions. A ~85% fraction of the telomeres showed a mobility that was restricted to average translocations of 0.36 ± 0.1 μm, whereas the remaining fraction of telomeres displayed an extended mobility described by a Gauss distribution centered around 0.8 ± 0.1 μm. For three telomeres r_c values of 1.35, 1.44, and 1.94 μm were determined. These data are not included in the histogram. (B) Summary of combined results from the telomere mobility analysis on the second, minute, and hour time scale, which yielded the indicated diffusion coefficients and translocation ranges (Figures 3 and 4).

Figure 6. FISH of telomere repeats. Metaphase chromosome spreads were hybridized with a Cy3-conjugated PNA probe against the telomere repeat sequence. The DNA was counterstained with DAPI. (A) Human lymphocytes showing a homogenous distribution of telomeres with repeats of 10–15 kb in length. (B) U2OS cell line, in which the alternative telomere lengthening (ALT) mechanism leads to large variations in telomere length. (C) FISH experiment conducted on metaphase chromosomes of the F6B2 clone using a fluorescently labeled probe coding for the *lac*O sequence. (D) Rehybridization of the metaphase spread shown in C with a Cy3-(CCCTAA)$_3$ PNA probe used for labeling the telomere repeats. (E) Examples for the comparison of telomere length as given by the intensity of the Cy3-PNA signal. The three different integration sites of *lac*O arrays were identified by FISH with a 6-FAM fluorescently labeled oligonucleotide probe against the *lac*O sequence. (F) Quantification of telomere length in U2OS (■) and HeLa cells (□) as derived from the intensity of the GFP-TRF2 fluorescence intensity signal. For normalization the integrated intensity of a given GFP-TRF2 spot was determined as the ratio to the average value of all GFP-TRF2 telomere signals in a given cell. The U2OS cells have a significantly higher amount of very short telomeres as reflected by the GFP-TRF2 signal ≤ 0.5. The two normalized distributions compare to absolute telomere repeat lengths in the range from <2 to ~23 kb reported for U2OS (Scheel *et al.,* 2001) and of 2–10 kb for HeLa cell lines (Bryan *et al.,* 1998). (G) Correlation of telomere mobility on the hour time scale as represented by the radius of accessible space versus the telomere repeat length as represented by the normalized GFP-TRF2 signal (see F). A total of 78 telomeres traced for ~3 h were evaluated. From the plot an inverse correlation of mobility with the telomere repeat length/GFP-TRF2 signal is apparent.

correlated with the fraction of telomeres that showed an extended mobility on the hour time scale. Telomeres were traced for 3–4 h in living cells that had a double-label of the telomeric *lac*O arrays with mRFP1-LacI and the telomere repeats via GFP-TRF2. From these trajectories the radius of the average accessible space was determined as described above and plotted against the corresponding telomere length as given by the normalized GFP-TRF2 signal. This analysis revealed an inverse correlation of the accessible space and the telomere repeat length/GFP-TRF2 signal, indicating that short telomeres indeed displayed an extended mobility (Figure 6G).

Mobility of PML Bodies in Relation to Telomeres

Cells of the F6B2 cell clone were cotransfected with GFP-PML III and mRFP1-LacI to examine the relation between telomere and PML-NB mobility. Immunostaining of endogenous PML protein showed that transient transfection of the cells with mRFP1-LacI did not modify number, size, or shape of PML-NBs compared with the cells used in this study. As expected, GFP-PMLIII colocalized with Sp100 protein, confirming that the corresponding structures were indeed PML-NBs (data not shown). Distinct telomere–PML-NB complexes, the APBs, were detected at 5–10% of the *lac*O-tagged telomeres (Figure 7, A–C). In three-color labeling experiments of *lac*O arrays, TRF2, and PML bodies, the APB structures were found with and without a TRF2 signal, indicating that APBs are present both at short and long telomeric repeats (data not shown). As evident from the enlarged view in Figure 7C, the APB complex was bigger than a normal PML-NB, and the PML protein adopted a cap-like structure around the telomere.

APBs formed via binding of an existing PML-NB to a telomere as visualized by the image series shown (Figure 7D, Supplemental Movie 8). In addition, a close inspection of the time-lapse series indicated that some free PML protein was also accumulating from the nucleoplasm around the telomere until the typical APB structure was established.

The PML-NB mobility with respect to the three telomeric *lac*O inserts was investigated by monitoring the change of distance between a PML-NB to the closest *lac*O array over time (Figure 8). The PML-NBs were referred to as PML$_b$, PML$_m$, and PML$_s$ according to the proximal *lac*O locus. Images of a typical experiment (Figure 8A, Supplemental Movie 9) and the corresponding plot of the squared distance change, Δd^2, for each three PML-telomere pairs are displayed in Figure 8B. Based on the analysis of 40 different trajectories, three types of PML mobility in addition to that of the APB complexes were observed. These are represented by the three curves of the averaged Δd^2 versus time relation in Figure 8C. Thus, four distinct types of PML body translocations were identified here: 1) PML bodies showing movements that were completely independent with respect to the proximal telomere-like PML$_m$ in Figure 8A. 2) PML bodies with a mobility fully correlated with that of the telomere but without direct colocalization to the telomere (PML$_b$ in Figure 8A). 3) PML bodies that displayed a movement, which partly correlated with that of the telomere (PML$_s$ in Figure 8A). 4) PML bodies forming an APB. As expected, this stable PML–telomere complex (Figure 7) also showed a completely correlated movement with the telomere (Supplemental Movie 10).
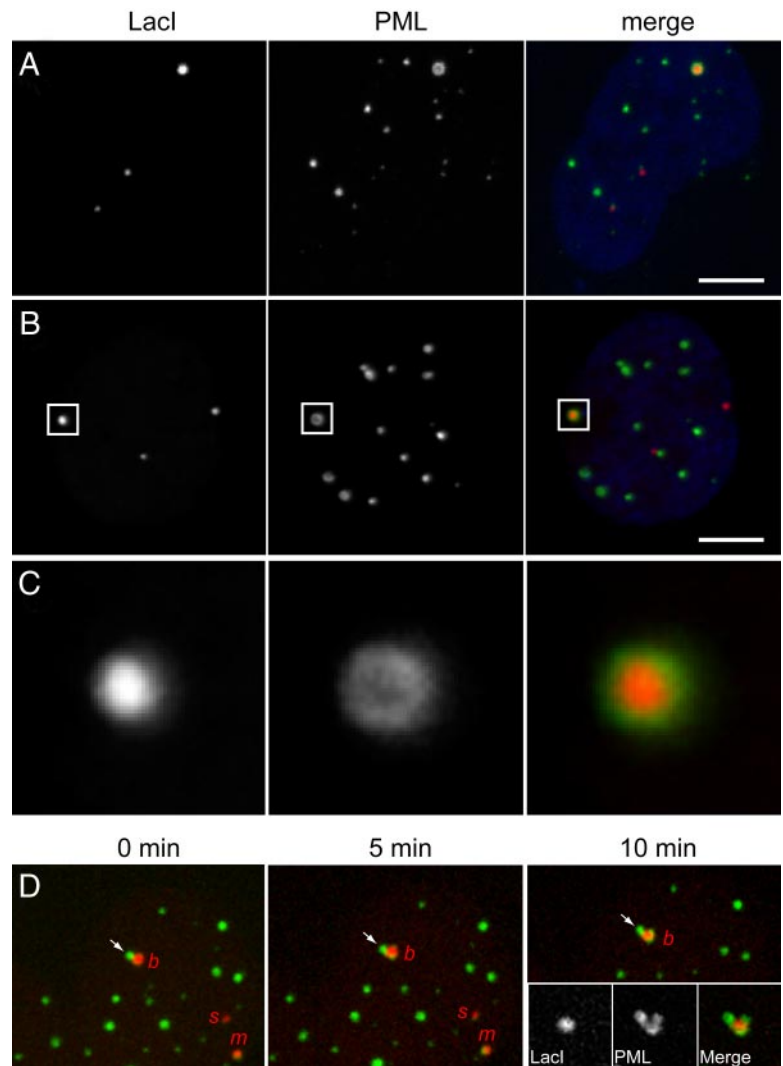
Figure 7. Structure of PML body-telomere complexes (APBs). (A) Cells were transiently transfected with mRFP1-LacI and fixed with PFA. PML bodies were stained with an antibody against PML protein together with an Alexa 488–coupled secondary antibody. Chromatin was stained with TO-PRO 3. (B) U2OS cell line F6B2 transiently cotransfected with mRFP1-LacI together with GFP-PML III. Cells were fixed with PFA, and chromatin was stained with TO-PRO 3. Scale bars, 5 μm. (C) Enlarged view of the PML complex at the telomere from the cell shown in B. The PML body formed a cap-like structure around the *lac*O/telomere label. (D) In the dual-color labeling experiments the formation of an APB complex could be visualized (Supplemental Movie 8).

DISCUSSION

Mobility of Telomeres in U2OS Cells

The mobility of chromatin loci as well as nuclear bodies has been examined in a number of studies as reviewed previously (Chuang and Belmont, 2007; Lanctôt *et al.*, 2007; Wachsmuth *et al.*, 2008). Here, a clone of the human U2OS cell line was investigated that had three *lac*O array integrations adjacent to the telomere of chromosomes 6q, 11p, and 12q. These could be distinguished in the in vivo experiments via bound GFP-LacI/mRFP1-LacI because of their different number of *lac*O repeats. A comprehensive model for telomere mobility was determined by combining measurements at the second, minute, and hour time scale that were all associated with different confinement radii for the telomere translocations (Figure 5B). By measuring the change of the distance between two labeled telomeres, instead of tracking a single telomere, the mobility measurements could be conducted with improved accuracy. On the minute time scale the *lac*O-tagged telomeres moved in a diffusive manner with $D_{min} = 4 \cdot 10^{-4} \ \mu m^2 \ s^{-1}$, similar to other chromatin loci, fluorescent centromeric protein clusters, or nuclear bodies, for which respective diffusion coefficients between $1.1 \cdot 10^{-4}$ and $1.8 \cdot 10^{-4} \ \mu m^2 \ s^{-1}$ were reported (Chubb *et al.*, 2002; Molenaar *et al.*, 2003; Görisch *et al.*, 2004). It is noted that the time

regime chosen for the experiments directly affects the resulting apparent diffusion coefficients, if for example, only the initial linear slope of the MSD versus time plot is evaluated (Wachsmuth *et al.*, 2008). In a high-resolution analysis the mobility of *lac*O arrays in Chinese hamster ovary (CHO) cells was measured on the second time scale (Levi *et al.*, 2005). Multiple mobility layers were detected, and the data were fitted to a confined diffusion model similar to the "moving corral" description used here (Equation 3). This analysis yielded $D_{fast} = 3.1 \cdot 10^{-3} \ \mu m^2 \ s^{-1}$ and $D_{slow} = 2.4 \cdot 10^{-4} \ \mu m^2 \ s^{-1}$, which is in good agreement with values of $D_{sec} = 2 \cdot 10^{-3} \ \mu m^2 \ s^{-1}$ and $D_{min} = 4 \cdot 10^{-4} \ \mu m^2 \ s^{-1}$ determined here for telomeres in U2OS cells.

Interestingly, at the hour time scale, the diffusion coefficient $D_{hour} = 1 \cdot 10^{-5} \ \mu m^2 \ s^{-1}$ derived from our analysis is very close to the one observed for 1-Mb chromatin domains labeled with Cy3-UTP on a similar time scale (Bornfleth *et al.*, 1999). This is consistent with the interpretation that this value represents the dynamics of large chromatin domains in the nucleus. The relatively low mobility measured for the majority of telomeres is also in agreement with a recent study where the mobility of DNA ends created from a double-strand break between a *lac*O/LacI-CFP and a *tet*O-TetR-YFP label was evaluated (Soutoglou *et al.*, 2007). The
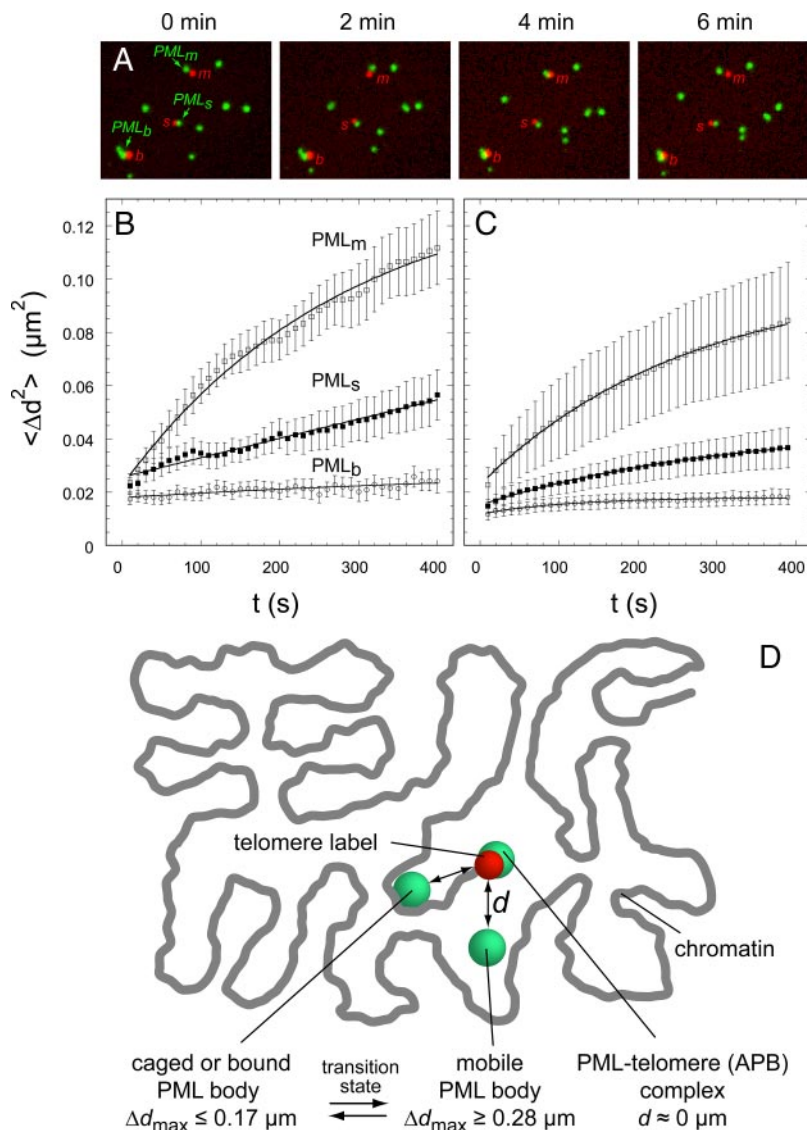
Figure 8. Relative mobility of PML bodies and telomeres. The U2OS cell line F6B2 was transiently cotransfected with GFP-PML III (green) and mRFP1-LacI (red). (A) The mobility of the three *lac*O inserts (*b*, *m*, and *s*) and proximal PML bodies was studied by recording changes in the relative distance between the spots (Supplemental Movie 9) and fitting these data to a confined diffusion model. (B) The mean squared changes $<\Delta d^2>$ in the distance between PML bodies and its proximal telomeres observed in the time lapse series of the cell shown in A were plotted against time. (C) Average mobility of PML-NBs with respect to a telomere with *lac*O label in close proximity, i.e., at a distance $\leq 1 \ \mu$m. Each curve represents averages of 10–15 measurements. About 20 cells were evaluated, and 30 PML-NBs plus ~10 APBs were traced with respect to the changes in the mean squared distance between telomere and PML signal. The results indicated a clustering of the trajectories into the three main groups shown. (D) Mobility of PML bodies close to telomeres ($d \leq 1 \ \mu$m). The experiments indicated the existence of four types of PML body movements: One group showed a mobility that was not correlated to that of the telomere ("mobile PML body"), whereas another group was clearly separated from the telomere but nevertheless followed the movements of the telomere. This suggests a confinement within or binding to the same chromatin region (caged or bound PML body). A third group displayed an intermediate behavior, i.e., a partial correlation of the translocations. The fourth class of PML bodies is represented by the APB complex with a stable association of PML body and telomere.

results indicate that DNA ends per se do not display a higher mobility than other chromatin loci. This supports the model of a linked chromatin fiber network, in which the local chromatin mobility is confined to a radius of a 150–250 nm (Wachsmuth *et al.*, 2008). In the analysis of the telomere mobility over 3–5 h two distinct populations were identified here (Figure 5A). Although ~85% of the telomeres moved within an average confinement radius of $0.36 \pm 0.16 \ \mu$m, the remaining fraction showed more extended translocations of $0.8 \pm 0.1 \ \mu$m. Furthermore, the size of the accessible region was inversely correlated with the length of the telomere repeat sequence (Figure 6). In a previous study the telomere mobility in U2OS cells was analyzed over a time period of 30–60 min with a 1-min time resolution after labeling the telomere repeats by hybridization with a PNA probe (Molenaar *et al.*, 2003). The majority of telomeres moved in a confined region with an apparent radius of ~0.5 μm and a short-range diffusion coefficient of $1.8\cdot10^{-4} \ \mu$m^2 s^{-1}, as inferred from the plateau and initial slope of the MSD versus time plot. A ~10% fraction of telomeres displayed a higher mobility for which translocations up to 1.2 μm and an apparent diffusion coefficient of $5.8\cdot10^{-4} \ \mu$m^2 s^{-1} were reported. The multiple time-scale analysis conducted here de-

scribed the telomere mobility by a model that provides a clear distinction between structural features of the nucleus environment (represented by the three different confinement radii) and the intrinsic telomere mobility (described by the corresponding three diffusion coefficients; Figure 5B). The previous conclusions on the existence of a fraction of telomeres with higher mobility were confirmed, albeit with some quantitative differences that are related both to the data analysis and the labeling method. It is noted that the in vivo PNA labeling approach allowed for the simultaneous detection of ~50% of the telomeres in the U2OS (Molenaar *et al.*, 2003). However, it is not suited for the analysis of the short telomeres that are characteristic for telomerase-negative cells, because these do not provide a signal of sufficient intensity for tracing them in vivo (Figures 2 and 6). Here, we were able to tag the chromosome ends via the *lac*O label so that the mobility of specific telomeres could be monitored independently of the telomere repeat length, albeit with the limitation to the simultaneous detection of only three telomeres.

Possible Origins of Increased Telomere Mobility

In yeast, telomeres and subtelomeric regions are attached to the nuclear envelope (Gotta *et al.*, 1996; Laroche *et al.*, 1998,

2000; Tham *et al.*, 2001; Hediger *et al.*, 2002). The analysis of in vivo mobility of chromosome VI-R, XIV-L, and VIII-L telomeres revealed relatively fast oscillating movements of 150–300 nm that could be assigned to an anchoring to the nuclear envelope via the Ku protein complex (Hediger *et al.*, 2002). In mammals telomeres appear randomly positioned in the nucleus during the G1 phase of the cell cycle (Luderus *et al.*, 1996; Chuang *et al.*, 2004; Ermler *et al.*, 2004), with some telomeres being specifically localized in heterochromatin at the nuclear and nucleolar periphery (Tam *et al.*, 2004). An association of telomeres with a nuclear matrix was suggested on the basis of biochemical approaches (Luderus *et al.*, 1996; Weipoltshammer *et al.*, 1999). However, the existence of the nuclear matrix remains controversial, and several lines of evidence support the view that a stable chromatin fiber network is established by different types of chromatin linkers so that no additional support structure is required (Rippe, 2007). Thus, a remaining more likely possibility is the association of telomeres with other chromatin domains.

Changes in the nuclear mobility of chromatin loci have also been reported in relation to the gene expression state. On activation of GAL genes in yeast a confinement of the GAL locus to a 2D sliding motion along the nuclear envelope was observed in live cell–imaging experiments (Cabal *et al.*, 2006). Furthermore, the results obtained here for telomere mobility bear some similarities with measurements of a VP16-inducible gene locus in CHO cells (Chuang *et al.*, 2006). The activation of the *lac*O-labeled gene region triggered a dramatic increase of its mobility, presumably by inducing its dissociation from a stable heterochromatin region. Interestingly, telomeres as well as subtelomeric regions display constitutive heterochromatin markers that tend to be lost upon shortening of telomere repeats (Benetti *et al.*, 2007). This type of anchoring could also include the self-association of different telomeres reported previously (Nagele *et al.*, 2001; Molenaar *et al.*, 2003; Chuang *et al.*, 2004). Here, we suggest that the higher mobility fraction of telomeres is characterized by a reduced ability to interact with other (hetero)chromatin regions to explain the inverse relation of telomere repeat length and mobility observed in our experiments. Interestingly, a recent study reports very similar behavior. The disruption of the telosome by deletion of TRF2 was found to increase telomere mobility in 53BP1-deficient cells by allowing them to sample larger nuclear territories (Dimitrova *et al.*, 2008).

PML Body Mobility in Relation to Telomeres

The comparison of telomere and PML-NB mobility is of interest in several aspects. First, it is an open question how mobile nuclear bodies and their associated activities could be targeted to a specific region of the nucleus (Muratani *et al.*, 2002; Platani *et al.*, 2002; Görisch *et al.*, 2004). We have reported previously that the PML-NB mobility in HeLa cells is indistinguishable from that of a bona fide inert particle, i.e., directly reflects the accessibility and dynamics of its chromatin environment (Görisch *et al.*, 2004). For the U2OS cell line this description is clearly inappropriate as specific complexes of PML-NBs with telomeres, the APBs, are formed that are not present in telomerase-positive cell lines like HeLa (Yeager *et al.*, 1999). Thus, a chromatin-bound state of PML-NBs exists in U2OS cells that appears to play an essential role in the ALT pathway (Yeager *et al.*, 1999; Nabetani *et al.*, 2004; Potts and Yu, 2007). With respect to the mobility of PML-NBs, four types were identified in our analysis (Figure 8D): 1) PML-NBs with translocations that were independent of a close telomere label. These were

confined to areas of an average radius of ~0.3 μm where they can diffuse freely with a mobility that was identical to those reported in HeLa cells (Görisch *et al.*, 2004). 2) PML-NBs that appeared to be stably associated with the same chromatin domain as the neighboring telomere, either by binding or by being trapped by the surrounding chromatin. These PML-NBs were observed at a distance of up to ~1 μm from the *lac*O label. 3) PML-NBs that had a correlated mobility with respect to the proximal telomere but, in addition, showed some independent translocations. These PML-NBs appear to represent an intermediate state between the completely mobile and the bound/caged group of PML-NBs, indicating that the transition between the two states is reversible on the minute time scale. 4) PML-NBs that form APBs as discussed below. The APB complexes did not dissociate on the time scale of the in vivo imaging experiments, and their formation was initiated by the interaction of a telomere with a preexisting PML-NB.

The mobility analysis conducted here does not reflect the absolute mobility of PML-NBs but their mobility relative to a proximal chromatin locus, i.e., the chromatin-independent part of their translocations. Accordingly, the apparent diffusion coefficients are relatively small and cannot be compared directly with the previously determined value of $D_{min,PML} = 2 \cdot 10^{-4}$ μm^2 s^{-1} from measurements on the minute time scale (Görisch *et al.*, 2004). The latter value is close to the corresponding measurement of $D_{min} = 4 \cdot 10^{-4}$ μm^2 s^{-1} determined here, suggesting that the translocations of PML-NBs mostly follow that of chromatin as proposed previously. In addition, the confinement radii for both PML-NBs and telomeres indicate that the typical size of the accessible region is limited to a radius of ~0.3 μm as reported previously for nuclear bodies and chromatin domains (Wachsmuth *et al.*, 2008). Thus, the data are consistent with a model in which chromatin dynamics, accessibility, and binding to (sub)telomeric chromatin loci determine the mobility of PML-NBs in ALT cells.

Structure and Formation of APBs

The PML protein is organized in a cap-like structure at the telomere that extends to the *lac*O array so that the chromosome end is covered with PML protein (Figure 7). In the 3D image reconstruction of APBs formed at the locus *b* of clone F6B2 (Supplemental Movie 7) the PML cap at the chromosome end appeared to extend to the neighboring fraction of the adjacent *lac*O repeats but did not encompass the whole array. Furthermore, the clone F4 2B8 with a *lac*O array integration close to the centromere (Figure 1D) displayed only an insignificant number of PML-NBs colocalizing with the *lac*O repeat (data not shown). These two observations indicate that PML-NBs do not have an affinity for the *lac*O repeat per se in U2OS cells as suggested previously in studies of a BHK cell line (Tsukamoto *et al.*, 2000). The PML cap-like structure around the telomere found in APBs, albeit smaller in size, is reminiscent of the unusually large PML-NBs that form in lymphocytes of patients affected with immunodeficiency, centromeric instability, and facial dysmorphy (ICF) syndrome (Luciani *et al.*, 2006). Interestingly, the hollow-spherical PML-NBs associated with the ICF syndrome contain a large amount of satellite DNA that displays the same repetitive nature and constitutive heterochromatin markers as the telomeric DNA in APBs. The *lac*O telomere in vivo labeling offered the unique opportunity to elucidate the formation process of an APB (Figure 7D, Supplemental Movie 8). A close examination of these data indicated that the APBs are formed in two steps: First, a preexisting PML-NB binds to the telomere and, in a second step, addi-

tional PML protein from the nucleoplasm is accumulated at this locus until the typical APB structure is formed. This two-stage process appears to be required because the typical PML content of the relatively large APBs significantly exceeds that of an isolated PML-NB.

A Model for the Mechanism of Alternative Telomere Lengthening

A valuable feature of the *lac*O/GFP-LacI telomere labeling in studies of the ALT system is the possibility to follow a specific telomere over time, independent of its repeat length. This type of analysis revealed an extended mobility of ~15% of the telomeres, whereas a similar fraction of 20–30% of the telomeres had telomere repeats that were too short to be detectable by FISH with the PNA probe (Figures 4–6). From a comparison with HeLa cells it is concluded that the presence of a high number of short telomeres is a characteristic feature of U2OS cells (Figure 6F). Furthermore, an inverse correlation of the confinement radius r_c and the telomere length was revealed (Figure 6G). Based on these findings and the results on telomere mobility and interaction with PML-NBs discussed above, the model in Figure 9 is proposed. The telosome protein complex at the intact telomere promotes interactions with other chromatin domains and mediates its anchoring within the nucleus. In this state the telomere mobility is low and similar to that of other chromatin loci. However, upon shortening of the telomere repeat below a certain threshold the telosome is disrupted, which could then release the telomere anchoring to allow for ex-
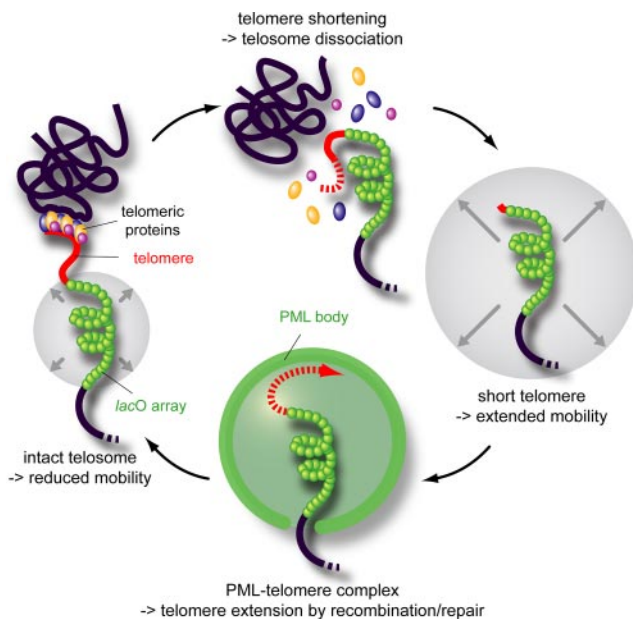

Figure 9. Model for telomere mobility and APB formation in the context of the ALT mechanism. In telomeres with sufficient repeat length the telosome protein complex mediates the anchoring to another chromatin domain. This results in a confined mobility of the telomere that is similar to that of other chromatin loci. When the telomere repeat length is reduced below a critical threshold, the telosome is disrupted, and the anchoring is lost. In this state the telomere displays a significantly extended mobility. The telomere associates with a PML body to form an APB complex, in which the telomere length is increased in a process that involves DNA recombination and repair. The telosome can reform on the extended telomere repeat sequence to reestablish the telomere anchoring associated with the reduced mobility state.

tended telomere translocations. Telomeres with short repeats and unprotected by the shelterin proteins TRF1, TRF2, and POT1 that directly recognize $(TTAGGG)_n$ sequence are likely to resemble the structure of DNA damage sites as discussed previously (de Lange, 2005). Interestingly, many proteins involved in the detection and the repair of double-strand breaks are found to accumulate, at least transiently, in PML bodies in general and also specifically in APBs (Dellaire and Bazett-Jones, 2004; Nabetani *et al.,* 2004; Bernardi and Pandolfi, 2007; Fasching *et al.,* 2007). Thus, the increased telomere mobility in conjunction with a double-strand break-like conformation of the chromosome end could favor both the formation of a stable APB complex as well as telomere–telomere interactions. It is apparent from the results obtained here that telomeres are recombination "hot spots" in U2OS cells. The vast majority clones constructed during this study (29 of 30) had the *lac*O arrays integrated at the telomeres. Moreover, the relatively large size of the *lac*O inserts obtained suggests the expansion of the integrated DNA. This could result from a pronounced DNA recombination and repair activity at the telomeres associated with the ALT pathway in the U2OS cell line (Dunham *et al.,* 2000; Kass-Eisler and Greider, 2000; Lundblad, 2002; Nabetani *et al.,* 2004; Muntoni and Reddel, 2005; Jiang *et al.,* 2007). Inasmuch as these activities are associated with the APB complex, it appears likely that its structure persists during the telomere lengthening process for some time as indicated in the scheme in Figure 9. When the number of repeats becomes sufficiently high the shelterin proteins can bind again to reestablish the telosome complex at the newly synthesized telomere repeat region. This would then promote interactions with other chromatin domains to induce a state of low mobility as observed for the majority of telomeres.

REFERENCES

Benetti, R., Garcia-Cao, M., and Blasco, M. A. (2007). Telomere length regulates the epigenetic status of mammalian telomeres and subtelomeres. Nat. Genet. *39*, 243–250.

Bernardi, R., and Pandolfi, P. P. (2007). Structure, dynamics and functions of promyelocytic leukaemia nuclear bodies. Nat. Rev. Mol. Cell Biol. *8*, 1006–1016.

Bertuch, A. A., and Lundblad, V. (2006). The maintenance and masking of chromosome termini. Curr. Opin. Cell Biol. *18*, 247–253.

Blasco, M. A. (2007). Telomere length, stem cells and aging. Nat. Chem. Biol. *3*, 640–649.

Bornfleth, H., Edelmann, P., Zink, D., Cremer, T., and Cremer, C. (1999). Quantitative motion analysis of subchromosomal foci in living cells using four-dimensional microscopy. Biophys. J. *77*, 2871–2886.

Bryan, T. M., Englezou, A., Dunham, M. A., and Reddel, R. R. (1998). Telomere length dynamics in telomerase-positive immortal human cell populations. Exp. Cell Res. *239*, 370–378.

Bryan, T. M., Englezou, A., Gupta, J., Bacchetti, S., and Reddel, R. R. (1995). Telomere elongation in immortal human cells without detectable telomerase activity. EMBO J. *14*, 4240–4248.

Cabal, G. G., *et al.* (2006). SAGA interacting factors confine sub-diffusion of transcribed genes to the nuclear envelope. Nature *441*, 770–773.

Chan, S. R., and Blackburn, E. H. (2004). Telomeres and telomerase. Philos. Trans. Roy. Soc. Lond. *359*, 109–121.

Chuang, C. H., and Belmont, A. S. (2007). Moving chromatin within the interphase nucleus-controlled transitions? Semin. Cell Dev. Biol. *18*, 698–706.

Chuang, C. H., Carpenter, A. E., Fuchsova, B., Johnson, T., de Lanerolle, P., and Belmont, A. S. (2006). Long-range directional movement of an interphase chromosome site. Curr. Biol. *16*, 825–831.

Chuang, T. C., *et al.* (2004). The three-dimensional organization of telomeres in the nucleus of mammalian cells. BMC Biol. *2*, 12.

Chubb, J. R., Boyle, S., Perry, P., and Bickmore, W. A. (2002). Chromatin motion is constrained by association with nuclear compartments in human cells. Curr. Biol. *12*, 439–445.

Collado, M., Blasco, M. A., and Serrano, M. (2007). Cellular senescence in cancer and aging. Cell *130*, 223–233.

Croy, J. E., and Wuttke, D. S. (2006). Themes in ssDNA recognition by telomere-end protection proteins. Trends Biochem. Sci. *31*, 516–525.

de Lange, T. (2005). Shelterin: the protein complex that shapes and safeguards human telomeres. Genes Dev. *19*, 2100–2110.

de Lange, T., Lundblad, V., and Blackburn, E. (2006). Telomeres, Cold Spring Harbor, NY: Cold Spring Harbor Laboratory Press.

Dellaire, G., and Bazett-Jones, D. P. (2004). PML nuclear bodies: dynamic sensors of DNA damage and cellular stress. Bioessays *26*, 963–977.

Dimitrova, N., Chen, Y. C., Spector, D. L., and de Lange, T. (2008). 53BP1 promotes non-homologous end joining of telomeres by increasing chromatin mobility. Nature *456*, 524–528.

Dunham, M. A., Neumann, A. A., Fasching, C. L., and Reddel, R. R. (2000). Telomere maintenance by recombination in human cells. Nat. Genet. *26*, 447–450.

Ermler, S., Krunic, D., Knoch, T. A., Moshir, S., Mai, S., Greulich-Bode, K. M., and Boukamp, P. (2004). Cell cycle-dependent 3D distribution of telomeres and telomere repeat-binding factor 2 (TRF2) in HaCaT and HaCaT-myc cells. Eur. J. Cell Biol. *83*, 681–690.

Fasching, C. L., Neumann, A. A., Muntoni, A., Yeager, T. R., and Reddel, R. R. (2007). DNA damage induces alternative lengthening of telomeres (ALT) associated promyelocytic leukemia bodies that preferentially associate with linear telomeric DNA. Cancer Res. *67*, 7072–7077.

Fejes Tóth, K., Knoch, T. A., Wachsmuth, M., Stöhr, M., Frank-Stöhr, M., Bacher, C. P., Müller, G., and Rippe, K. (2004). Trichostatin A induced histone acetylation causes decondensation of interphase chromatin. J. Cell Sci. *117*, 4277–4287.

Gilson, E., and Geli, V. (2007). How telomeres are replicated. Nat. Rev. Mol. Cell Biol. *8*, 825–838.

Görisch, S. M., Wachsmuth, M., Ittrich, C., Bacher, C. P., Rippe, K., and Lichter, P. (2004). Nuclear body movement is determined by chromatin accessibility and dynamics. Proc. Natl. Acad. Sci. USA *101*, 13221–13226.

Gotta, M., Laroche, T., Formenton, A., Maillet, L., Scherthan, H., and Gasser, S. M. (1996). The clustering of telomeres and colocalization with Rap1, Sir3, and Sir4 proteins in wild-type *Saccharomyces cerevisiae.* J. Cell Biol. *134*, 1349–1363.

Greider, C. W., and Blackburn, E. H. (1985). Identification of a specific telomere terminal transferase activity in *Tetrahymena* extracts. Cell *43*, 405–413.

Harley, C. B., Futcher, A. B., and Greider, C. W. (1990). Telomeres shorten during ageing of human fibroblasts. Nature *345*, 458–460.

Hediger, F., Neumann, F. R., Van Houwe, G., Dubrana, K., and Gasser, S. M. (2002). Live imaging of telomeres: yKu and Sir proteins define redundant telomere-anchoring pathways in yeast. Curr. Biol. *12*, 2076–2089.

Jiang, W. Q., Zhong, Z. H., Henson, J. D., and Reddel, R. R. (2007). Identification of candidate alternative lengthening of telomeres genes by methionine restriction and RNA interference. Oncogene *26*, 4635–4647.

Johnson, J. E., and Broccoli, D. (2007). Telomere maintenance in sarcomas. Curr. Opin. Oncol. *19*, 377–382.

Kass-Eisler, A., and Greider, C. W. (2000). Recombination in telomere-length maintenance. Trends Biochem. Sci. *25*, 200–204.

Lanctôt, C., Cheutin, T., Cremer, M., Cavalli, G., and Cremer, T. (2007). Dynamic genome architecture in the nuclear space: regulation of gene expression in three dimensions. Nat. Rev. Genet. *8*, 104–115.

Lansdorp, P. M., Verwoerd, N. P., van de Rijke, F. M., Dragowska, V., Little, M. T., Dirks, R. W., Raap, A. K., and Tanke, H. J. (1996). Heterogeneity in telomere length of human chromosomes. Hum. Mol. Genet. *5*, 685–691.

Laroche, T., Martin, S. G., Gotta, M., Gorham, H. C., Pryde, F. E., Louis, E. J., and Gasser, S. M. (1998). Mutation of yeast Ku genes disrupts the subnuclear organization of telomeres. Curr. Biol. *8*, 653–656.

Laroche, T., Martin, S. G., Tsai-Pflugfelder, M., and Gasser, S. M. (2000). The dynamics of yeast telomeres and silencing proteins through the cell cycle. J. Struct. Biol. *129*, 159–174.

Lau, I. F., Filipe, S. R., Soballe, B., Okstad, O. A., Barre, F. X., and Sherratt, D. J. (2003). Spatial and temporal organization of replicating *Escherichia coli* chromosomes. Mol. Microbiol. *49*, 731–743.

Leonhardt, H., Rahn, H. P., Weinzierl, P., Sporbert, A., Cremer, T., Zink, D., and Cardoso, M. C. (2000). Dynamics of DNA replication factories in living cells. J. Cell Biol. *149*, 271–280.

Levi, V., Ruan, Q., Plutz, M., Belmont, A. S., and Gratton, E. (2005). Chromatin dynamics in interphase cells revealed by tracking in a two-photon excitation microscope. Biophys. J. *89*, 4275–4285.

Luciani, J. J., *et al.* (2006). PML nuclear bodies are highly organised DNA-protein structures with a function in heterochromatin remodelling at the G2 phase. J. Cell Sci. *119*, 2518–2531.

Luderus, M. E., van Steensel, B., Chong, L., Sibon, O. C., Cremers, F. F., and de Lange, T. (1996). Structure, subnuclear distribution, and nuclear matrix association of the mammalian telomeric complex. J. Cell Biol. *135*, 867–881.

Lundblad, V. (2002). Telomere maintenance without telomerase. Oncogene *21*, 522–531.

Marshall, W. F., Straight, A., Marko, J. F., Swedlow, J., Dernburg, A., Belmont, A., Murray, A. W., Agard, D. A., and Sedat, J. W. (1997). Interphase chromosomes undergo constrained diffusional motion in living cells. Curr. Biol. *7*, 930–939.

Martens, U. M., Chavez, E. A., Poon, S. S., Schmoor, C., and Lansdorp, P. M. (2000). Accumulation of short telomeres in human fibroblasts prior to replicative senescence. Exp. Cell Res. *256*, 291–299.

Molenaar, C., Wiesmeijer, K., Verwoerd, N. P., Khazen, S., Eils, R., Tanke, H. J., and Dirks, R. W. (2003). Visualizing telomere dynamics in living mammalian cells using PNA probes. EMBO J. *22*, 6631–6641.

Muntoni, A., and Reddel, R. R. (2005). The first molecular details of ALT in human tumor cells. Hum. Mol. Genet. *14*(Spec No. 2), R191–R196.

Muratani, M., Gerlich, D., Janicki, S. M., Gebhard, M., Eils, R., and Spector, D. L. (2002). Metabolic-energy-dependent movement of PML bodies within the mammalian cell nucleus. Nat. Cell Biol. *4*, 106–110.

Nabetani, A., Yokoyama, O., and Ishikawa, F. (2004). Localization of hRad9, hHus1, hRad1, and hRad17 and caffeine-sensitive DNA replication at the alternative lengthening of telomeres-associated promyelocytic leukemia body. J. Biol. Chem. *279*, 25849–25857.

Nagele, R. G., Velasco, A. Q., Anderson, W. J., McMahon, D. J., Thomson, Z., Fazekas, J., Wind, K., and Lee, H. (2001). Telomere associations in interphase nuclei: possible role in maintenance of interphase chromosome topology. J. Cell Sci. *114*, 377–388.

Neumann, A.A., and Reddel, R.R. (2006). Telomerase-independent maintenance of mammalian telomeres. In: Telomeres, eds. T. de Lange, V. Lundblad, and E. Blackburn, Cold Spring Harbor, NY: Cold Spring Harbor Laboratory Press, 163–198.

Perrem, K., Colgin, L. M., Neumann, A. A., Yeager, T. R., and Reddel, R. R. (2001). Coexistence of alternative lengthening of telomeres and telomerase in hTERT-transfected GM847 cells. Mol. Cell. Biol. *21*, 3862–3875.

Platani, M., Goldberg, I., Lamond, A. I., and Swedlow, J. R. (2002). Cajal body dynamics and association with chromatin are ATP-dependent. Nat. Cell Biol. *4*, 502–508.

Possoz, C., Filipe, S. R., Grainge, I., and Sherratt, D. J. (2006). Tracking of controlled *Escherichia coli* replication fork stalling and restart at repressor-bound DNA in vivo. EMBO J. *25*, 2596–2604.

Potts, P. R., and Yu, H. (2007). The SMC5/6 complex maintains telomere length in ALT cancer cells through SUMOylation of telomere-binding proteins. Nat. Struct. Mol. Biol. *14*, 581–590.

Reymann, J., Baddeley, D., Gunkel, M., Lemmer, P., Stadter, W., Jegou, T., Rippe, K., Cremer, C., and Birk, U. (2008). High precision structural analysis of subnuclear complexes in fixed and living specimens via spatially modulated illumination (SMI) microscopy. Chromosome Res. *16*, 367–382.

Rippe, K. (2007). Dynamic organization of the cell nucleus. Curr. Opin. Genet. Dev. *17*, 373–380.

Robinett, C. C., Straight, A., Li, G., Willhelm, C., Sudlow, G., Murray, A., and Belmont, A. S. (1996). In vivo localization of DNA sequences and visualization of large-scale chromatin organization using lac operator/repressor recognition. J. Cell Biol. *135*, 1685–1700.

Sage, D., Neumann, F. R., Hediger, F., Gasser, S. M., and Unser, M. (2005). Automatic tracking of individual fluorescence particles: application to the study of chromosome dynamics. IEEE Trans. Image Process. *14*, 1372–1383.

Scheel, C., Schaefer, K. L., Jauch, A., Keller, M., Wai, D., Brinkschmidt, C., van Valen, F., Boecker, W., Dockhorn-Dworniczak, B., and Poremba, C. (2001). Alternative lengthening of telomeres is associated with chromosomal instability in osteosarcomas. Oncogene *20*, 3835–3844.

Soutoglou, E., Dorn, J. F., Sengupta, K., Jasin, M., Nussenzweig, A., Ried, T., Danuser, G., and Misteli, T. (2007). Positional stability of single double-strand breaks in mammalian cells. Nat. Cell Biol. *9*, 675–682.

Straight, A. F., Belmont, A. S., Robinett, C. C., and Murray, A. W. (1996). GFP tagging of budding yeast chromosomes reveals that protein-protein interactions can mediate sister chromatid cohesion. Curr. Biol. *6*, 1599–1608.

Takahashi, Y., Lallemand-Breitenbach, V., Zhu, J., and de The, H. (2004). PML nuclear bodies and apoptosis. Oncogene *23*, 2819–2824.

Tam, R., Smith, K. P., and Lawrence, J. B. (2004). The 4q subtelomere harboring the FSHD locus is specifically anchored with peripheral heterochromatin unlike most human telomeres. J. Cell Biol. *167*, 269–279.

Tham, W. H., Wyithe, J. S., Ko Ferrigno, P., Silver, P. A., and Zakian, V. A. (2001). Localization of yeast telomeres to the nuclear periphery is separable from transcriptional repression and telomere stability functions. Mol. Cell *8*, 189–199.

Thévenaz, P., Ruttimann, U. E., and Unser, M. (1998). A pyramid approach to subpixel registration based on intensity. IEEE Trans. Image Process. *7*, 27–41.

Tsukamoto, T., Hashiguchi, N., Janicki, S. M., Tumbar, T., Belmont, A. S., and Spector, D. L. (2000). Visualization of gene activity in living cells. Nat. Cell Biol. *2*, 871–878.

Vazquez, J., Belmont, A. S., and Sedat, J. W. (2001). Multiple regimes of constrained chromosome motion are regulated in the interphase *Drosophila* nucleus. Curr. Biol. *11*, 1227–1239.

Wachsmuth, M., Caudron-Herger, M., and Rippe, K. (2008). Genome organization: Balancing stability and plasticity. Biochim. Biophys. Acta *1783*, 2061–2079.

Weidemann, T., Wachsmuth, M., Knoch, T. A., Muller, G., Waldeck, W., and Langowski, J. (2003). Counting nucleosomes in living cells with a combination of fluorescence correlation spectroscopy and confocal imaging. J. Mol. Biol. *334*, 229–240.

Weidtkamp-Peters, S., *et al.* (2008). Dynamics of component exchange at PML nuclear bodies. J. Cell Sci. *121*, 2731–2743.

Weipoltshammer, K., Schofer, C., Almeder, M., Philimonenko, V. V., Frei, K., Wachtler, F., and Hozak, P. (1999). Intranuclear anchoring of repetitive DNA sequences: centromeres, telomeres, and ribosomal DNA. J. Cell Biol. *147*, 1409–1418.

Yeager, T. R., Neumann, A. A., Englezou, A., Huschtscha, L. I., Noble, J. R., and Reddel, R. R. (1999). Telomerase-negative immortalized human cells contain a novel type of promyelocytic leukemia (PML) body. Cancer Res. *59*, 4175–4179.

SUPPLEMENTARY MATERIAL

Dynamics of telomeres and PML nuclear bodies in a telomerase negative human cell line

Thibaud Jegou[*,§], Inn Chung[*,§], Gerrit Heuvelman[*,§], Malte Wachsmuth[||], Sabine M. Görisch[†], Karin M. Greulich-Bode[‡], Petra Boukamp[‡], Peter Lichter[†] & Karsten Rippe[*,§]

Deutsches Krebsforschungszentrum, [*]Research Group Genome Organization & Function, [†]Division of Molecular Genetics and [‡]Division of Genetics of Skin Carcinogenesis, Im Neuenheimer Feld 280, 69120 Heidelberg, Germany; [§]BioQuant, Im Neuenheimer Feld 267, 69120 Heidelberg, Germany; [||]European Molecular Biology Laboratory, Cell Biology/Biophysics Unit, Meyerhofstr. 1, 69117 Heidelberg, Germany

Address correspondence to: Karsten Rippe, Tel.: +49-6221-54-51376, Fax: +49-6221-54-51487, e-mail: Karsten.Rippe@bioquant.uni-heidelberg.de

Supplemental Text

Analysis of telomere mobility from distance changes between telomeres

To evaluate particle translocations by diffusion the square of the distance $\vec{p}_i(t+\Delta t) - \vec{p}_i(t)$ between the two positions $\vec{p}_i(t)$ and $\vec{p}_i(t+\Delta t)$ of the particle i before and after a time Δt is measured, averaged for all identical values of Δt and then plotted against the time difference Δt. This yields the mean squared displacement

$$MSD_i(\Delta t) = \left\langle \left[\vec{p}_i(t+\Delta t) - \vec{p}_i(t) \right]^2 \right\rangle \tag{S1}$$

The accurate measurement of particle mobility in the nucleus is difficult as also the cell itself can move or the microscope stage can show drift during the measurement, and the alignment to correct for this is difficult. In general, when considering two particles, their positions can be decomposed into mutually independent contributions from diffusion, translation of their center point, and rotation around their center point:

$$\vec{p}_i(t) = \vec{p}_{i,\mathrm{diff}}(t) + \vec{p}_{i,\mathrm{trans}}(t) + \vec{p}_{i,\mathrm{rot}}(t) \quad (i = 1,2) \tag{S2}$$

Usually, the diffusion process on the one hand and the translational and rotational movement on the other hand take place on different time and length scales so that they can both be approximated as linear motion on the characteristic time scales of the diffusion process. While the diffusive contributions of different spots or particles are mutually independent, the translational and rotational contributions obey:

$$\vec{p}_{1,\mathrm{trans}}(t + \Delta t) - \vec{p}_{1,\mathrm{trans}}(t) = \vec{p}_{2,\mathrm{trans}}(t + \Delta t) - \vec{p}_{2,\mathrm{trans}}(t) = \vec{p}_{\mathrm{trans}}(t + \Delta t) - \vec{p}_{\mathrm{trans}}(t)$$
$$\vec{p}_{1,\mathrm{rot}}(t + \Delta t) - \vec{p}_{1,\mathrm{rot}}(t) = -\left[\vec{p}_{2,\mathrm{rot}}(t + \Delta t) - \vec{p}_{2,\mathrm{rot}}(t)\right] = \vec{p}_{\mathrm{rot}}(t + \Delta t) - \vec{p}_{\mathrm{rot}}(t) \tag{S3}$$

Hence, it can be shown that the mean squared displacement of each of the two particles can be decomposed into:

$$MSD_i(\Delta t) = MSD_{i,\mathrm{diff}}(\Delta t) + MSD_{\mathrm{trans}}(\Delta t) + MSD_{\mathrm{rot}}(\Delta t) \tag{S4}$$

with the contributions

$$MSD_{i,\mathrm{diff}}(\Delta t) = \left\langle \left[\vec{p}_{i,\mathrm{diff}}(t + \Delta t) - \vec{p}_{i,\mathrm{diff}}(t)\right]^2 \right\rangle$$
$$MSD_{\mathrm{trans}}(\Delta t) = \left\langle \left[\vec{p}_{\mathrm{trans}}(t + \Delta t) - \vec{p}_{\mathrm{trans}}(t)\right]^2 \right\rangle \tag{S5}$$
$$MSD_{\mathrm{rot}}(\Delta t) = \left\langle \left[\vec{p}_{\mathrm{rot}}(t + \Delta t) - \vec{p}_{\mathrm{rot}}(t)\right]^2 \right\rangle$$

In order to eliminate the translational contribution, we measured changes in the distance $\vec{d}(t) = \vec{p}_1(t) - \vec{p}_2(t)$ between two loci as an observable. With Eq. S2 and S3, the corresponding mean squared distance change MSΔD turns out to be:

$$MS\Delta D(\Delta t) = \left\langle \left[\vec{d}(t + \Delta t) - \vec{d}(t)\right]^2 \right\rangle$$
$$= \left\langle \left\{\left[\vec{p}_{1,\mathrm{diff}}(t + \Delta t) - \vec{p}_{1,\mathrm{diff}}(t)\right] - \left[\vec{p}_{2,\mathrm{diff}}(t + \Delta t) - \vec{p}_{2,\mathrm{diff}}(t)\right] + 2\left[\vec{p}_{\mathrm{rot}}(t + \Delta t) - \vec{p}_{\mathrm{rot}}(t)\right]\right\}^2 \right\rangle$$
$$= \left\langle \left[\vec{p}_{1,\mathrm{diff}}(t + \Delta t) - \vec{p}_{1,\mathrm{diff}}(t)\right]^2 \right\rangle + \left\langle \left[\vec{p}_{2,\mathrm{diff}}(t + \Delta t) - \vec{p}_{2,\mathrm{diff}}(t)\right]^2 \right\rangle + 4\left\langle \left[\vec{p}_{\mathrm{rot}}(t + \Delta t) - \vec{p}_{\mathrm{rot}}(t)\right]^2 \right\rangle$$
$$= MSD_{1,\mathrm{diff}}(\Delta t) + MSD_{2,\mathrm{diff}}(\Delta t) + 4 MSD_{\mathrm{rot}}(\Delta t) \tag{S6}$$

In the case studied here, the translational displacement of the cell was significant but the rotational contribution was negligible ($MSD_{\mathrm{rot}}(\Delta t) \approx 0$). Thus, $MS\Delta D$ is given by the

sum of the single particle mean squared displacements. In the case of a significant rotational contribution, the center point $\vec{s}(t) = \vec{p}_1(t) + \vec{p}_2(t)$ can serve as observable, yielding the corresponding mean squared displacement:

$$
\begin{aligned}
MS\Sigma D(\Delta t) &= \left\langle \left[\vec{s}(t+\Delta t) - \vec{s}(t) \right]^2 \right\rangle \\
&= \left\langle \left\{ \left[\vec{p}_{1,\mathrm{diff}}(t+\Delta t) - \vec{p}_{1,\mathrm{diff}}(t) \right] + \left[\vec{p}_{2,\mathrm{diff}}(t+\Delta t) - \vec{p}_{2,\mathrm{diff}}(t) \right] + 2\left[\vec{p}_{\mathrm{trans}}(t+\Delta t) - \vec{p}_{\mathrm{trans}}(t) \right] \right\}^2 \right\rangle \\
&= \left\langle \left[\vec{p}_{1,\mathrm{diff}}(t+\Delta t) - \vec{p}_{1,\mathrm{diff}}(t) \right]^2 \right\rangle + \left\langle \left[\vec{p}_{2,\mathrm{diff}}(t+\Delta t) - \vec{p}_{2,\mathrm{diff}}(t) \right]^2 \right\rangle + 4\left\langle \left[\vec{p}_{\mathrm{trans}}(t+\Delta t) - \vec{p}_{\mathrm{trans}}(t) \right]^2 \right\rangle \\
&= MSD_{1,\mathrm{diff}}(\Delta t) + MSD_{2,\mathrm{diff}}(\Delta t) + 4 MSD_{\mathrm{trans}}(\Delta t)
\end{aligned}
$$

(S7)

$MS\Sigma D$ represents the sum of the single particle mean squared displacements when the translational contribution can be neglected.

In order to verify whether the rotational or the translational contribution are negligible, we used the mean linear displacement of the difference or the sum of the two particle positions, respectively. The diffusive contribution vanishes and we obtain:

$$
\begin{aligned}
M\Delta\vec{D}(\Delta t) &= \left\langle \left[\vec{d}(t+\Delta t) - \vec{d}(t) \right] \right\rangle \\
&= \left\langle \left[\vec{p}_{1,\mathrm{diff}}(t+\Delta t) - \vec{p}_{1,\mathrm{diff}}(t) \right] - \left[\vec{p}_{2,\mathrm{diff}}(t+\Delta t) - \vec{p}_{2,\mathrm{diff}}(t) \right] + 2\left[\vec{p}_{\mathrm{rot}}(t+\Delta t) - \vec{p}_{\mathrm{rot}}(t) \right] \right\rangle \\
&= \left\langle \vec{p}_{1,\mathrm{diff}}(t+\Delta t) - \vec{p}_{1,\mathrm{diff}}(t) \right\rangle - \left\langle \vec{p}_{2,\mathrm{diff}}(t+\Delta t) - \vec{p}_{2,\mathrm{diff}}(t) \right\rangle + 2\left\langle \vec{p}_{\mathrm{rot}}(t+\Delta t) - \vec{p}_{\mathrm{rot}}(t) \right\rangle \\
&= 0 - 0 + 2\vec{v}_{\mathrm{rot}}\Delta t
\end{aligned}
$$

(S8)

based on the assumption that the rotational contribution can be approximated as linear motion with velocity $\vec{v}_{\mathrm{rot}}$ whereas the mean squared displacement contribution yields $MSD_{\mathrm{rot}}(\Delta t) = \left(\vec{v}_{\mathrm{rot}}\Delta t \right)^2$. Therefore, when $M\Delta\vec{D} = 0$, Eq. S6 can be used to determine the sum of the diffusive contributions of the two particles or spots under investigation. In analogy, we find:

$$
\begin{aligned}
M\Sigma\vec{D}(\Delta t) &= \left\langle \left[\vec{s}(t+\Delta t) - \vec{s}(t) \right] \right\rangle \\
&= \left\langle \left[\vec{p}_{1,\mathrm{diff}}(t+\Delta t) - \vec{p}_{1,\mathrm{diff}}(t) \right] + \left[\vec{p}_{2,\mathrm{diff}}(t+\Delta t) - \vec{p}_{2,\mathrm{diff}}(t) \right] + 2\left[\vec{p}_{\mathrm{trans}}(t+\Delta t) - \vec{p}_{\mathrm{trans}}(t) \right] \right\rangle \\
&= \left\langle \vec{p}_{1,\mathrm{diff}}(t+\Delta t) - \vec{p}_{1,\mathrm{diff}}(t) \right\rangle + \left\langle \vec{p}_{2,\mathrm{diff}}(t+\Delta t) - \vec{p}_{2,\mathrm{diff}}(t) \right\rangle + 2\left\langle \vec{p}_{\mathrm{trans}}(t+\Delta t) - \vec{p}_{\mathrm{trans}}(t) \right\rangle \\
&= 0 + 0 + 2\vec{v}_{\mathrm{trans}}\Delta t
\end{aligned}
$$

(S9)

and $MSD_{\mathrm{trans}}(\Delta t) = \left(\vec{v}_{\mathrm{trans}}\Delta t \right)^2$ where $\vec{v}_{\mathrm{trans}}$ is the translational velocity. When $M\Sigma\vec{D} = 0$, Eq.

S7 can be used to determine the sum of the diffusive contributions of the two particles or spots under investigation. In the experiments reported here the translational displacement of the cell was significant but the rotational contribution was negligible ($MSD_{rot}(\Delta t) \approx 0$) so that Eq. S6 yields:

$$MS\Delta D(\Delta t) = MSD_{1,\text{diff}}(\Delta t) + MSD_{2,\text{diff}}(\Delta t) \qquad \text{(S10)}$$

Accordingly, for free diffusion in *n* dimensions we obtain

$$MS\Delta D_{\text{free}} = 2n\left(D_1 + D_2\right)\Delta t \qquad \text{(S11)}$$

To describe the restricted mobility of particles in the nucleus we have previously introduced a so called "moving corral" (MC) model (Görisch et al., 2005; Görisch et al., 2004) shown in Eq. S12. An analysis of the data on the mobility of *lac*O loci indicated that a similar approach was also appropriate to represent the mobility of telomeres on different length and time scales.

$$MSD_{\text{MC}} = \left\langle r_c^2 \right\rangle \cdot \left(1 + \frac{2n\,D_{\text{slow}}\,\Delta t}{\left\langle r_c^2 \right\rangle}\right) \cdot \left[1 - \exp\left(-\frac{2n\,D_{\text{fast}}\,\Delta t}{\left\langle r_c^2 \right\rangle}\right)\right] \qquad \text{(S12)}$$

In the MC model the overall mobility is determined by three parameters: The particle experiences fast but confined diffusion with a coefficient D_{fast} in a corral with radius r_c. These corrals can also translocate according to a free diffusion model with a diffusion coefficient D_{slow}. If the corrals do not translocate, i.e. for $D_{\text{slow}} = 0$ one obtains Eq. S13 for the diffusion displacement of the particle that is confined to a corral, where $\left\langle r_c^2 \right\rangle$ is the long term *MSD*:

$$MSD_{\text{cor}} = \left\langle r_c^2 \right\rangle \cdot \left[1 - \exp\left(-\frac{2n\,D_{\text{fast}}\,\Delta t}{\left\langle r_c^2 \right\rangle}\right)\right] \qquad \text{(S13)}$$

When applying this relation to evaluate the change in the distance between two particles that experience corralled diffusion Eq. S14 is obtained:

$$MS\Delta D_{cor} = \left\langle r_{c,1}^{\,2} \right\rangle \cdot \left[1 - \exp\left(-\frac{2n\,D_{fast,1}\,\Delta t}{\left\langle r_{c,1}^{\,2} \right\rangle} \right) \right] + \left\langle r_{c,2}^{\,2} \right\rangle \cdot \left[1 - \exp\left(-\frac{2n\,D_{fast,2}\,\Delta t}{\left\langle r_{c,2}^{\,2} \right\rangle} \right) \right] \qquad (S14)$$

This equation was used for the description of telomere mobility on the hour time scale. By conducting a global fit of the distances between telomeres 1 and 2, 1 and 3 and 2 and 3 in a given cell. The values of $r_{c,1}$, $r_{c,2}$, $r_{c,3}$, $D_{fast,1}$, $D_{fast,2}$ and $D_{fast,3}$ were derived. For the case that $D_{fast,1}/\left\langle r_{c,1}^{\,2} \right\rangle \approx D_{fast,2}/\left\langle r_{c,2}^{\,2} \right\rangle$ with a difference of the two ratios smaller than a factor of 3, Eq. S14 can be well approximated as:

$$MS\Delta D_{cor} \approx \left(\left\langle r_{c,1}^{\,2} \right\rangle + \left\langle r_{c,2}^{\,2} \right\rangle \right) \cdot \left[1 - \exp\left(-\frac{2n\left(D_{fast,1} + D_{fast,2}\right)\Delta t}{\left\langle r_{c,1}^{\,2} \right\rangle + \left\langle r_{c,2}^{\,2} \right\rangle} \right) \right] \qquad (S15)$$

As the translocation of the corrals in the MC model is represented by a free diffusion term that is described by Eq. S11 for MSΔD, the above relations can be combined into Eq. S16.

$$MS\Delta D_{MC} \approx \left(\left\langle r_{c,1}^{\,2} \right\rangle + \left\langle r_{c,2}^{\,2} \right\rangle \right) \cdot \left(1 + \frac{2n\left(D_{slow,1} + D_{slow,2}\right)\Delta t}{\left(\left\langle r_{c,1}^{\,2} \right\rangle + \left\langle r_{c,2}^{\,2} \right\rangle \right)} \right) \cdot \left[1 - \exp\left(-\frac{2n\left(D_{fast,1} + D_{fast,2}\right)\Delta t}{\left(\left\langle r_{c,1}^{\,2} \right\rangle + \left\langle r_{c,2}^{\,2} \right\rangle \right)} \right) \right] \quad (S16)$$

This relation was found to be a good representation of the telomere mobility on the second and minute time scale. The fit to Eq. S16 was conducted with three parameters $r_c = r_{c,1} + r_{c,2}$, $D_{slow} = D_{slow,1} + D_{slow,2}$ and $D_{fast} = D_{fast,1} + D_{fast,2}$ for each of the distances 1-2, 2-3 and 1-3. These corresponded to the distance between telomeres b and m (b-m), b and s (b-s) and m and s (m-s) (Fig. 2B). The values retrieved from the fit were then decomposed to determine the individual values of each telomere by solving the equation system:

$$\left\langle r_{c,1\text{-}2}^{\,2} \right\rangle = \left\langle r_{c,1}^{\,2} \right\rangle + \left\langle r_{c,2}^{\,2} \right\rangle \quad \left\langle r_{c,2\text{-}3}^{\,2} \right\rangle = \left\langle r_{c,2}^{\,2} \right\rangle + \left\langle r_{c,3}^{\,2} \right\rangle \quad \left\langle r_{c,1\text{-}3}^{\,2} \right\rangle = \left\langle r_{c,1}^{\,2} \right\rangle + \left\langle r_{c,3}^{\,2} \right\rangle$$

$$D_{slow,1\text{-}2} = D_{slow,1} + D_{slow,2} \quad D_{slow,2\text{-}3} = D_{slow,2} + D_{slow,3} \quad D_{slow,1\text{-}3} = D_{slow,1} + D_{slow,3} \qquad (S17)$$

$$D_{fast,1\text{-}2} = D_{fast,1} + D_{fast,2} \quad D_{fast,2\text{-}3} = D_{fast,2} + D_{fast,3} \quad D_{fast,1\text{-}3} = D_{fast,1} + D_{fast,3}$$

Supplemental Figures and movies

Fig. S1. The complexity of the U2OS karyotype leads to some uncertainties in the identification of the chromosome into which the *lac*O repeat was inserted. Therefore, multicolor fluorescence in situ hybridization (mFISH) experiments followed by *lac*O FISH re-hybridization were conducted. This procedure allowed a more reliable identification of the chromosomes. In clone F6B2 the three different sized *lac*O arrays (*b*, *m*, *s*) were found to integrate at the telomeric regions of chromosomes 11p, 6q and 12q. (A) mFISH analysis. (B) Metaphase FISH using a 6-FAM fluorescently labeled oligonucleotide probe coding for the *lac*O sequence and DNA counter-staining with DAPI. (C) Different color channels of mFISH analysis for the three chromosomes that showed *lac*O integration. The *lac*O array sequence appears to give an unspecific signal in the "Gold" and "Aqua" channel (Fig. S1 C). According to the mFISH color key this combination is specific for the "Y" chromosome. Since the U2OS cell line is derived from a female patient this artefact is unlikely to interfere with the mFISH data interpretation.

Movie 1. Co-mobility of *lac*O integrations and TRF2 labeled telomere repeats

http://malone.bioquant.uni-heidelberg.de/publications/MBC_movies/movie_01.mov

After a double transfection of F6B2 cells with mRFP1-LacI and GFP-TRF2 a z-axis stack of the two cells shown was recorded every 5 min. The video displays maximum intensity projections of the resulting pictures. Both *b* loci and the *s* locus of the upper cell co-localized with GFP-TRF2 foci in a single confocal plan. A correlated mobility between these *lac*O arrays and the associated GFP-TRF2 signal is apparent and was confirmed in a quantitative analysis (data not shown). Other telomeres as for example the *m* locus in the bottom cell did not co-localize with a GFP-TRF2 spot. This indicates the presence of a short telomere repeat at this chromosome.

Movie 2. Cell cycle analysis with the replication associated protein PCNA

http://malone.bioquant.uni-heidelberg.de/publications/MBC_movies/movie_02.mov

Cells were co-transfected with mRFP1-LacI and the replication associated protein PCNA fused to CFP to distinguish cells in G1 phase and in S phase according to the appearance of PCNA in replication foci. In the movie two cells with a clear PCNA-CFP signal are shown over a period of 180 min. On the first frame, both cells are in G1 phase as evident from the diffuse PCNA pattern. Then the upper cell progresses into S phase where PCNA becomes localized into replication foci. In this type of experiments an arrest in early S phase by LacI repressor was observed that prevented the duplication of the lacO repeat and further progression through S phase and cell division.

Movie 3. Mobility of telomeres on the second time scale

http://malone.bioquant.uni-heidelberg.de/publications/MBC_movies/movie_03.mov

A cell is displayed with the three *lac*O inserts visualized by bound GFP-LacI. Images were recorded every 80 ms and the movie reflects the approximate real-time mobility of the *lac*O loci.

Movie 4. Mobility of telomeres on the minute time scale

http://malone.bioquant.uni-heidelberg.de/publications/MBC_movies/movie_04.mov

Z-axis picture stacks of the GFP-LacI tagged telomeres were recorded every 10 seconds. The movie displays an exemplary cell in maximum intensity projections of the picture stacks at an ~25x increased speed.

Movie 5. Mobility of telomeres on the hour time scale (majority of telomere)

http://malone.bioquant.uni-heidelberg.de/publications/MBC_movies/movie_05.mov

Cells were transiently transfected with a plasmid coding for GFP-LacI. The 3D images were recorded every 5 minutes and maximum intensity projections of a time lapse series is shown. The movie plays at an ~700x increased speed. A confined mobility of

telomeres similar to that shown in the movie was observed in the majority of the telomeres trajectories.

Movie 6. Extended mobility of some telomeres on the hour time scale

http://malone.bioquant.uni-heidelberg.de/publications/MBC_movies/movie_06.mov

Imaging was conducted as described in the legend to Supplemental Movie 5. The selected cell displayed two of the three telomeres (*b* and *s* loci) with a highly extended mobility, while telomere *m* is only moderately mobile.

Movie 7. Three dimensional image of an ALT associated PML body (APB)

http://malone.bioquant.uni-heidelberg.de/publications/MBC_movies/movie_07.mov

Double transfection with mRFP1-LacI and GFP-PML III to label telomeres and PML bodies. Cells were fixed with PFA and chromatin was stained with TO-PRO 3. A z-axis stack with 0.3 µm distance between each picture was recorded from which the 3D reconstruction was generated. In the APB the PML body formed a cap-like structure around the *lac*O/telomere label of locus *b*.

Movie 8. Formation of an APB

http://malone.bioquant.uni-heidelberg.de/publications/MBC_movies/movie_08.mov

Time-lapse live imaging of mRFP1-LacI and GFP-PML III tagged cells. A z-axis picture stack was recorded every 10 seconds with a spinning disk confocal laser scanning microscope. The video shows maximum intensity projections of the picture stacks. The formation of an APB was initiated by binding of an existing PML body to the *lac*O labeled telomere. Then PML protein from the nucleoplasm accumulated at the partially formed APB structure until the APB complex was complete.

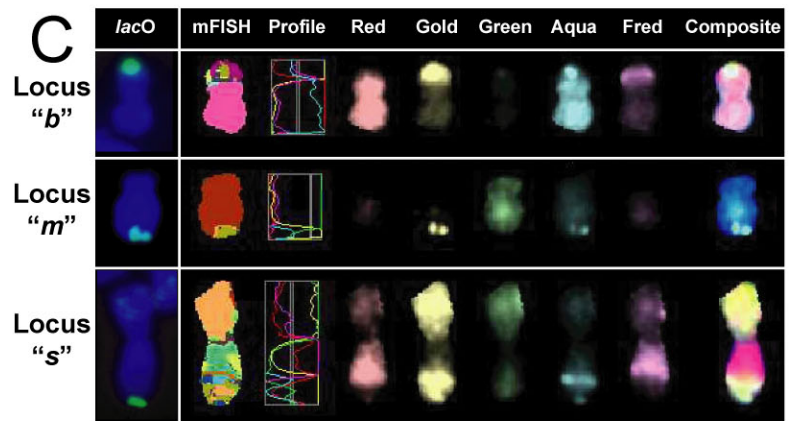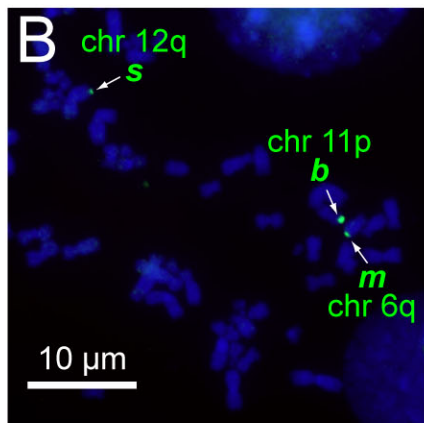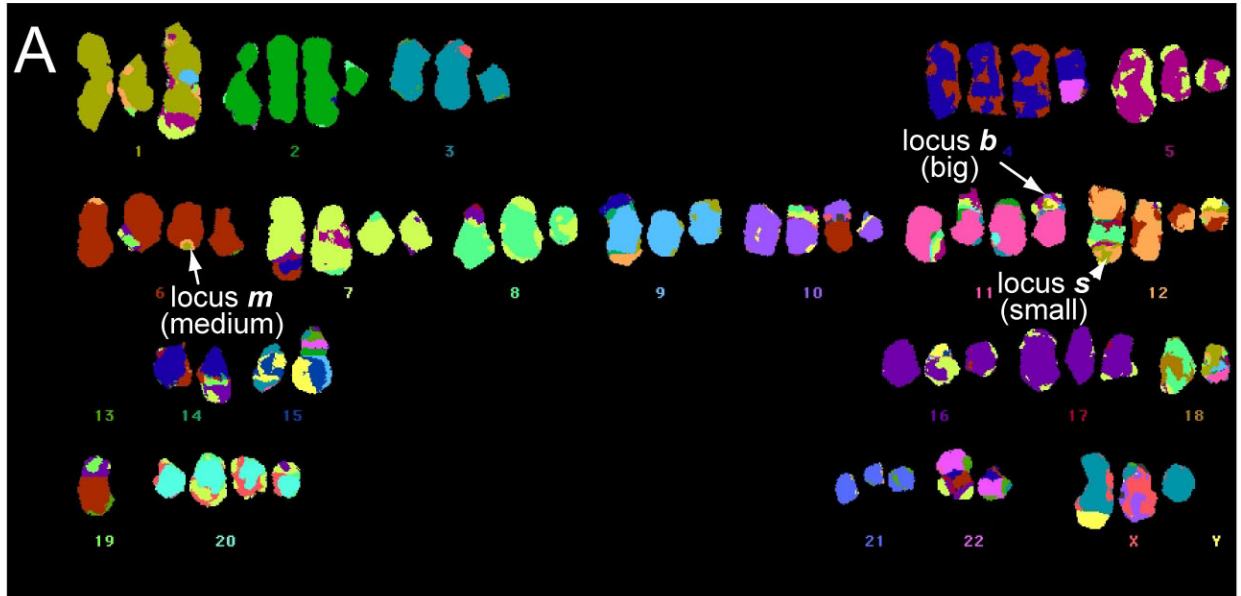**Movie 9. Relative mobility of PML bodies and telomeres**

http://malone.bioquant.uni-heidelberg.de/publications/MBC_movies/movie_09.mov

Imaging was conducted as described in the legend to Supplemental Movie 8. The mobility of PML bodies relative to a *lac*O labeled telomere in close proximity (≤ 1 µm) was monitored over time by measuring the distance change between them.

Movie 10. APB mobility

http://malone.bioquant.uni-heidelberg.de/publications/MBC_movies/movie_10.mov

Imaging was conducted as described in the legend to Supplemental Movie 8. In the video the mobility of an APB in the upper right side of the nucleus at telomere locus *m* was traced over a period of ~10 minutes.

A

locus **b**
(big)

locus **m**
(medium)

locus **s**
(small)

B

chr 12q
s

chr 11p
b

chr 6q
m

10 μm

C

	*lac*O	mFISH	Profile	Red	Gold	Green	Aqua	Fred	Composite
Locus "**b**"									
Locus "**m**"									
Locus "**s**"									

Supplemental Fig. S1, Jegou et al.